DE GRUYTER OPEN Curved and Layer. Struct. 2015; 2:59–90

Review Article **Open Access**

Rossana Dimitri*

Isogeometric treatment of large deformation contact and debonding problems with T-splines: a review

Abstract: Within a setting where the isogeometric analysis (IGA) has been successful at bringing two different research fields together, i.e. Computer Aided Design (CAD) and numerical analysis, T-spline IGA is applied in this work to frictionless contact and mode-I debonding problems between deformable bodies in the context of large deformations. Based on the concept of IGA, the smooth basis functions are adopted to describe surface geometries and approximate the numerical solutions, leading to higher accuracy in the contact integral evaluation. The isogeometric discretizations are here incorporated into an existing finite element framework by using Bézier extraction, i.e. a linear operator which maps the Bernstein polynomial basis on Bézier elements to the global isogeometric basis. A recently released commercial T-spline plugin for Rhino is herein used to build the analysis models adopted in this study.

In such context, the continuum is discretized with cubic T-splines, as well as with Non Uniform Rational B-Splines (NURBS) and Lagrange polynomial elements for comparison purposes, and a Gauss-point-to-surface (GPTS) formulation is combined with the penalty method to treat the contact constraints. The purely geometric enforcement of the non-penetration condition in compression is generalized to encompass both contact and mode-I debonding of interfaces which is approached by means of cohesive zone (CZ) modeling, as commonly done by the scientific community to analyse the progressive damage of materials and interfaces. Based on these models, non-linear relationships between tractions and relative displacements are assumed. These relationships dictate both the work of separation per unit fracture surface and the peak stress that has to be reached for the crack formation. In the generalized GPTS formulation an automatic switching procedure is used to choose between cohesive and contact models, depending on the contact status. Some numerical results are first presented and compared in 2D for varying resolutions of the contact and/or cohesive zone, including frictionless sliding and cohesive debonding, all featuring the competitive accuracy and performance of T-spline IGA. The superior accuracy of T-spline interpolations with respect to NURBS and Lagrange interpolations for a given number of degrees of freedom (Dofs) is always verified. The isogeometric formulation is also extended to 3D bodies, where some examples in large deformations based on T-spline discretizations show an high smoothness of the reaction history curves.

DOI 10.1515/cls-2015-0005
Received December 15, 2014; accepted January 5, 2015

1 Introduction

Computational contact or fracture analysis in the regime of finite deformations has received much attention in recent years owing to its great relevance in many fields of engineering and applied sciences. Some examples are: the interaction between soil and foundations in civil engineering, general bearing problems as well as bolt and screw joints, or the interfacial debonding of laminated materials and structures in mechanical, micro-electronic and aerospace engineering. Both contact and debonding problems are still two challenging topics in computational mechanics because of their nonlinear nature and their high sensitivity to the geometry accuracy.

Contact

Within contact formulations, C^0-continuous finite element basis functions often lead to undefined or non-uniquely defined normals at the inter-element boundaries which can cause some serious problems of convergence, both in a 2D and 3D setting [1,2] especially in the analyses of large sliding contact. This is mainly due to the non-smooth variation of the contact kinematic and kinetic variables because of the sliding movement of the slave nodes

---

***Corresponding Author: Rossana Dimitri:** Department of Innovation Engineering, University of Salento, Lecce, Italy

(i.e. nodes on the contact surface) over subsequent master facets (facets of the counteraprt contact surface), and the consequent abrupt changes of the contact forces causing unphysical oscillations in the results and failure of a standard Newton-Raphson iterative scheme.

In order to alleviate these effects, different geometrical smoothing techniques have been proposed in the literature for 2D and 3D deformable solids in contact, based on Hermite [3-5], Bézier [6-8], Spline interpolations [5], subdivision surfaces [9, 10] and NURBS interpolations [11]. Smoothing procedures improve the performance of the contact algorithms by increasing the continuity of the contact master surface and providing a unique definition of the normal and tangent vector across the master element boundaries, although the geometrical smoothness of the slave boundaries remains unaltered.

These procedures operate only on the contact surface, leaving the bulk descriptions of the interacting solids away from the contact zone unchanged, thereby introducing an inconsistency between bulk and surface responses. Moreover, smoothing often introduces complications in the implementation and data management due to the linearization of the relationship between real and smoothed geometries for implicit computations, and can in some cases compromise the sparse structure of the stiffness matrix [5]. On the other hand, the robustness of contact computations also depends on an accurate and smooth decription of the global and local contact interactions (i.e. the contact pressures).

The advent of IGA, as introduced recently in [12], has provided the context in which an exact description of the geometry is combined with the possible achievement of the desired degree of continuity at the element boundaries, as well as with additional advantageous features including variation diminishing and convex hull properties, and non-negativeness of the basis function. IGA can be regarded as a successful merging of two disparate research communities: that of CAD and that of numerical analysis. Coverting CAD models into a form suitable for analysis is considered a laborious task, usually dominating the design process. A direct route is provided by IGA for which the functions adopted to describe CAD surfaces are often directly amenable for analysis where properties such as partition of unity, linear independence, non-negativity and weak Kronecker delta property can be proven. By using the exact geometry and based on the advantageous properties of the basis functions that are used in CAD, several important developments have been made in the computational mechanics community.

Some investigations on contact mechanics in the framework of IGA have been recently conducted in [13-20], where 2D and 3D, frictional and frictionless problems have been solved by means of different contact formulations, based on a different description and enforcement of the contact conditions. An extended overview of the isogeometric contact methods available thus far in the literature is presented in [21], where two important features are comparatively analysed, such as the contact patch test performance and the stability of each algorithm.

More specifically, an accurate satisfaction of a mortar IGA-based thermomechanical frictionless contact constraints is observed in [13] even at coarse resolutions in 2D and 3D. The pressure distributions are evaluated for a classical Hertz contact problem, and found considerably smoother than those arising from Lagrange discretizations. Similar efforts are pursued also in [15] by using an interface NURBS-based fitting example. In [16] the authors also demonstrate the higher efficiency of NURBS geometries than Lagrange interpolations to describe 2D frictional problems, both in terms of local stress distributions and global force histories. The magnitude of the non-physical oscillations is shown, through a simple ironing problem, to decrease with increasing order of NURBS discretizations, whereas it tends to increase with increasing order of Lagrange polynomials eventually leading to loss of convergence.

A 3D mortar-based frictional contact treatment in IGA with NURBS is presented in [14], where the high quality of the local contact traction distributions is demonstrated for a deformable-to-rigid contact problem, followed by some global evaluations of force-time histories in the contact of deformable bodies.

Similar results for 3D applications are obtained in [17] where an exact enforcement of the contact constraints is obtained by using the AL method as proposed in [22]. This approach is characterized by a remarkable degree of robustness and yields an symptotically quadratic convergence rate. Small and large contact deformation problems are performed by the authors and the quality of the contact pressures is shown to improve over that achieved with Lagrange discretizations. In detail, the contact pressure distributions stemming from NURBS parameterizations result to be always non-negative and practically insensitive to the interpolation order. On the contrary, the local pressure distributions and global time-histories obtained from Lagrange parameterizations are sensitive to the interpolation order, display spurious oscillations and can attain significant non-physical negative values. From the standpoint of the solution method, a comparison between AL and penalty is performed in [22] which confirms the superiority of the former in terms of robustness and iterative convergence behaviour, in addition to the advantage of the exact contact constraints enforcement.

An example of point collocation approach within an isogeometric node-to-surface (NTS) formulation is given in [18] within a 2D frictionless setting. The contact integrals are collocated in this case at a set of physical points in one-to-one correspondence with the control points associated to the surface, as e.g. the Greville and Botella abscissae of the knot vectors. A convergence study of the Hertzian problem shows better results for a contact area near the patch boundary Greville points. A frictionless contact formulation suitable for isogeometric collocation has been recently proposed in [20] and shown to pass the contact patch test and deliver accurate results also for highly non-uniform meshes. Within isogeometric collocation, contact constraints are treated as deformation-dependent Neumann boundary conditions on the active contact portion of the boundary, which may be identified with classical active set strategies.

Based on the first results in the literature, the NURBS-based contact formulation provide a robust description of large deformation contact between deformable bodies, which is both effective and accurate for different interpolation orders. This implies that the unification of the geometric modeling and analysis phases proposed in [12,23] can be extended to mechanical problems in which contact phenomena occur. The following step, pursued in this work, is the extension of the contact formulation to T-spline discretizations, which enable local refinement and waterproof merging of different patches [24].

T-spline interpolations are herein adopted to model 2D and 3D large deformation frictionless contact problems between deformable bodies, in comparison to NURBS and Lagrange discretizations. Within a general finite element framework, where isogeometric interpolations are introduced through Bézier extraction, the contact contribution to the variational formulation in the discretized setting is computed using a simple Gauss-point-to-surface (GPTS) approach, previously introduced for linear and quadratic Lagrange elements [25] and extended to NURBS [13,16]. The frictionless contact constraints are regularized by the penalty method. Some numerical examples demonstrate the potential of T-spline IGA to solve challenging contact problems in 2D and 3D. In particular, an ironing problem is used as a benchmark to compare the performance of T-splines with NURBS and Lagrange discretizations from the standpoint of spatial convergence.

Fracture

In the context of fracture and debonding problems, the traditional finite element methods have shown many difficulties dealing with crack propagation problems because of the mesh regeneration adapted to the moving boundaries and the singularity near the crack tip. The development of damage at the interfaces results in formation and growth of interlaminar cracks through a non-linear and irreversible process which is known as debonding. Efficient and robust numerical tools verified by dedicated experiments are required to predict debonding initiation and its growth pattern under complex thermo-hygro-mechanical loading conditions that may arise during the lifetime of a laminated or jointed structure. It facilitates a prior assessment of the system reliability and performance without a need to perform experiments in individual cases.

Different numerical approaches have been proposed in the literature for the analysis of debonding initiation and propagation. Interface stress is commonly used as a failure criterion in an interface fracture mechanics based on finite element analysis of debonding. In stress-based approaches, stress at the interface is compared to the critical stress levels to indicate the interfacial regions most prone to debonding. Such methods assume perfect adhesion between materials, without considering the defect state, and overestimate the loading capacity. The brittle fracture of microsystems, for example, is usually characterized by a small fracture process zone (FPZ), such that the linear elastic fracture mechanics (LEFM) concepts can be applied [26,27].

Finite element-based techniques such as J-integral [28], virtual crack closure (VCC) [29,30], and virtual crack extension (VCE) [31] have been introduced in the literature within the LEFM framework for the prediction of debonding. The simplified Griffith energy balance considers the storage of the mechanical energy supplied to the system, as an elastic internal energy or dissipated through generating new crack surfaces [32]. Based on this concept, debonding propagates when the energy available for crack propagation exceeds the fracture toughness, or the critical energy release rate, which is a mechanical parameter of the interface. The complexity of a crack propagation process additionally increases in the case of a mixed-mode debonding as a transverse shear in the contact zone of a crack tip can raise the energy required for failure [33-35]. Another drawback of this class of methods is that explicit knowledge of the location and size of an initial crack is necessary. Moreover, a high mesh density in the crack front region is usually required to capture the singularity in the asymptotic crack tip fields with the conventional finite element method.

In enriched FEM, incorporating the asymptotic crack tip fields in the trial functions allows for an accurate computation of fracture parameters [36,37]. However, the meshing and remeshing as the crack grows represents a major drawback of LEFM approaches. In order to avoid the mesh regeneration, finite elements with embedded discontinuities and the Element Free Galerkin method (EFGM) have been successfully applied to crack problems [38,39], which is a mesh free method, with the smooth moving least square basis. The extended finite element method (XFEM) can withstand well the problems associated with discontinuity of the displacement field across the crack faces. To avoid a non-physical singular stress field at the crack tip, the crack growth is accompanied by a cohesive law on crack faces using the partition of unity property of finite elements [40,41]. In a XFEM based approach, however, the crack tip position is usually prescribed inside an element, allowing to determine the elements to be enriched by a discontinuous function or by near-tip asymptotic functions [42]. As as alternative, the discontinuity is often extended across a complete element such that the crack tip touches the next element boundary. Due to the oscillatory nature of the singular stress in the vicinity of the crack tip, appropriate crack tip asymptotic displacement functions are added to the finite element approximation for bi-material interface cracks [43]. Although a qualitative impression of the most vulnerable interface in a jointed system can be provided by comparing the crack driving forces in several interfaces, it is too hard to describe the cases where some cracks may be arrested or evolve simultaneously even in 2D problems when adopting LEFM-based methods. In addition, none of these methods are able to simulate both initiation and propagation of debonding together.

Due to the appealing feature of predicting both the debonding onset and its growth, CZ models have been increasingly used as numerical tool to simulate debonding as a result of the progressive decay of cohesive forces and the formation of traction-free surfaces between two materials or laminated structures where the potential cracks are known a priori [44,45]. CZ models have been originally introduced in [46] and [47] as an alternative to elasticity-based fracture mechanics, which leads to infinite stresses at the crack tip, in perfectly elastic-brittle materials. These models have been used to describe a broad range of fracture and damage processes in a wide variety of materials, such as ductile [48-52] or composite materials [45, 53-57].

The numerical application of CZ models for debonding problems within finite element frameworks suffers from an intrinsic discretization sensitivity. Coarse mesh discretizations of a cohesive crack, for instance, may lead to a sudden release of the elastic strain energy in large CZ elements, causing a sequence of non physical snap-through or snap-back points in the global load-deflection response, and compromising the numerical efficiency at the meantime [58]. As debonding propagates, indeed, there should be a sufficient interface elements in the softening FPZ to capture well the strain field.

To this end, remedies such as the artificial reduction of the interfacial strength with an increasing size of the FPZ using viscous regularization techniques and using a non-local formulation for the interface model are either unrealistic or computationally inefficient and expensive. A current solution strategy with respect to this problem aims at eliminating or reducing the oscillations. Since the observed oscillations are discretization-induced, they are alleviated through mesh refinement, without yielding unrealistic results. Therefore, the element size has to be extremely small for realistic interface parameters with a small FPZ size, which results in unacceptably high computational costs.

In contrast to refinement of the entire domain, local refinement of the FPZ is a computationally more efficient alternative. To this end, different surface enrichment strategies have been developed in the literature using different types of enrichment functions for CZ interface elements [59,60], as well as for contact elements [30].

The advent of IGA, however, provides a framework in which an exact description of geometries, an higher order of continuities and local refinement strategies may limit or avoid completely the above mentioned numerical problems. Local isogeometric refinement techniques include, T-splines [24,61-64], truncated hierarchical B-splines (THB-splines) [65], polynomial splines over hierarchical T-meshes (PHT-splines) [66], and locally-refineable splines (LR-splines) [67].

This paper presents, in the second part, a simple isogeometric framework for the 2D and 3D analysis of interfaces undergoing contact and cohesive debonding (see also [68]). These two phenomena are here treated within a unified framework, by developing an IGA-based generalized contact element which embeds the enforcement of the non-penetration contact conditions in compression as well as a bilinear mode-I CZ model in tension. The generalized contact element allows for non-matching discretizations of the interacting surfaces, as well as for large deformation cases where the interacting bodies undergo significant relative displacements in the normal and tangential directions.

The continuum is discretized with cubic T-splines, as well as with NURBS and Lagrange polynomial elements for comparison purposes. Some numerical examples demonstrate the potential of IGA to solve debonding problems in 2D and 3D. In particular, the double cantilver beam (DCB) test with even bending moments is first used as benchmark to compare the performance of Lagrange and NURBS discretizations, for varying interpolation order, with T-splines. The same formulation is then adopted to analyse 2D and 3D peeling and debonding contact problems. The superior accuracy of T-spline interpolations with respect to NURBS and Lagrange ones for a given number of Dofs is always verified.

2 IGA preliminaries

In this section the basic notions of IGA are overwied for both NURBS and T-spline interpolations. For additional details the interested reader is referred to [12, 24, 61,62, 69-71].

2.1 B-Splines, NURBS

Knot vectors and B-spline basis

The B-spline parametric space is local to *patches* rather than elements. Patches play the role of *subdomains* within which element types and material models are assumed to be uniform. A knot vector in one dimension is a sequence in ascending order of parameter values, written $\Xi = \{\xi_1, \xi_2, \ldots, \xi_{n+p+1}\}$ where ξ_A is the Ath knot, A is the knot index, $A = 1, 2, \ldots, n+p+1$, p is the order of the B-spline basis, and n is the number of basis functions which comprise the B-spline. Given a knot vector Ξ, the B-spline basis functions are defined recursively by the Cox-de Boor recursion formula starting with the zeroth order basis function ($p = 0$) given by

$$N_{A,0}(\xi) = \begin{cases} 1 & \xi_A \le \xi < \xi_{A+1} \\ 0 & otherwise \end{cases} \tag{1}$$

For $p = 1, 2, 3, \ldots$, they are defined by using the Cox-de Boor recursion formula

$$N_{A,p}(\xi) = \frac{\xi - \xi_A}{\xi_{A+p} - \xi_A} N_{A,p-1}(\xi) + \frac{\xi_{A+p+1} - \xi}{\xi_{A+p+1} - \xi_{A+1}} N_{A+1,p-1}(\xi) \tag{2}$$

B-splines are characterized by the following properties:

- *Partition of unity*

$$\sum_{A=1}^{n} N_{A,p}(\xi) = 1 \qquad \xi \in [\xi_1, \xi_{n+p+1}] \tag{3}$$

- *Pointwise nonnegativity*

$$N_{A,p}(\xi) \ge 0 \qquad A = 1, 2, \ldots, n \tag{4}$$

- *Linear independence*

$$\sum_{A=1}^{n} c_A N_{A,p}(\xi) = 0 \Leftrightarrow c_B = 0 \quad B = 1, 2, n \tag{5}$$

- *Compact support*

$$\left\{ \xi \mid N_{A,p}(\xi) > 0 \right\} \subset \left[\xi_A, \xi_{A+p+1} \right] \tag{6}$$

- *Control of continuity.* If ξ_A has multiplicity k (i.e., $\xi_A = \xi_{A+1} = \ldots = \xi_{A+k+1}$), then the basis functions are C^{p-k}-continuous at ξ_A. When $k = p$, the basis is C^0 and interpolatory at the location.

These features are useful in a finite element context. The first four properties above mentioned ensure a well conditioned and sparse stiffness matrix. The last property allows continuity to be reduced to better resolve steep gradients, while the higher continuity leads to superior accuracy per Dof compared with C^0-continuous bases [11, 72, 73]. Additionally, B-splines can be used to build a basis that spans the same space as classical p-version finite elements (i.e., a basis of order p that is C^0 across element boundaries). This is the well-known Bernstein basis [74].

B-spline curve

B-spline curves in $\mathbb{R}^{d_s}$ are constructed by taking a linear combination of B-spline basis functions, where d_s is the spatial dimension. The coefficients of the basis functions are referred to as *control points,* which are analogous to the nodal coordinates in finite element analysis. Piecewise linear interpolation of the control points gives the so-called *control polygon*. Generally control points are not interpolated by B-spline curves. Given n basis functions, $\mathbf{N} = \left\{ N_{A,p} \right\}_{A=1}^{n}$ and the corresponding control points $\mathbf{P} = \{\mathbf{P}_A\}_{A=1}^{n}$, a piecewise-polynomial *B-spline curve* is given by

$$\mathbf{C}(\xi) = \sum_{A=1}^{n} \mathrm{N}_{A,p}(\xi)\, \mathbf{P}_A \tag{7}$$

Important properties of B-spline curves can be summarized as follows

- They have continuous derivatives of order $p - 1$ in the absence of repeated knots or control points.
- The number of continuous derivatives by k is decreased by repeating a knot or control point k times.

- An affine transformation of a B-spline curve is obtained by applying the transformation to the control points. This property is referred as *affine covariance*.

B-spline curves also maintain all the continuity properties of their supporting bases. As visible in Fig. 1, for example, the curve is interpolatory at the first and last control points, for an open knot vector, and also at the sixth control point, for a multiplicity of the knot equal to the polynomial order.

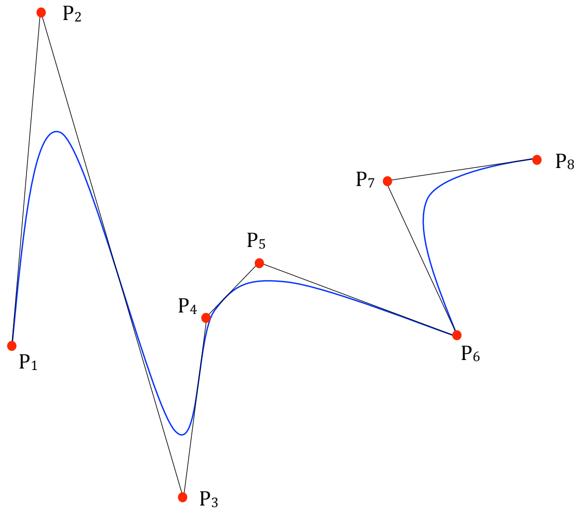

Figure 1: B-spline piecewise quadratic curve in $\mathbb{R}^2$.

NURBS curves

Given a knot vector $\Xi = \{\xi_1, \xi_2, \ldots \xi_{n+p+1}\}$, a set of rational basis functions $\mathbf{R} = \{R_{A,p}\}_{A=1}^{n}$, and a set of control points $\mathbf{P} = \{\mathbf{P}_A\}_{A=1}^{n}$, a NURBS can be defined as

$$\mathbf{C}(\xi) = \sum_{A=1}^{n} \mathrm{R}_{A,p}(\xi)\,\mathbf{P}_A \tag{8}$$

where NURBS basis functions are defined as

$$\mathrm{R}_{A,p}(\xi) = \frac{N_{A,p}(\xi)\, w_A}{W(\xi)} = \frac{N_{A,p}(\xi)\, w_A}{\sum_{B=1}^{n} N_{B,p}(\xi)\, w_B} \tag{9}$$

A rational curve in $\mathbb{R}^n$ can be obtained by projective trasformations of B-spline curves in the projective space $\mathbb{P}^n$. This means that if $\mathbf{P}_A$ is a control point of a NURBS curve, the corresponding control point in the projective space is $\tilde{\mathbf{P}}_A = \{w_A \mathbf{P}_A, w_A\}^T$. Therefore, given a NURBS curve defined in $\mathbb{R}^n$ by eq.(8), the corresponding B-spline curve defined in $\mathbb{P}^n$ is

$$\mathbf{C}(\xi) = \sum_{A=1}^{n} \mathrm{N}_{A,p}(\xi)\,\tilde{\mathbf{P}}_A \tag{10}$$

In this way the algorithms operating on B-splines can be applied to NURBS. Selecting appropriate values for the w_A permits the description of many different types of curves including polynomials and circular arches. For the special case in which $w_A = constant$, $A = 1, 2, \ldots n$ the NURBS basis reduces to the B-spline one. For simple geometries, the weights can be defined analytically [75], whereas for complex geometries, they are obtained from CAD packages such as Rhino [76].

NURBS surfaces and solids

A mapping $\tilde{A}$ is now introduced between the tensor product space and the global indexing of the basis functions and control points in order to maintain the following single-index notation for T-splines. Let $i = 1, 2, \ldots, n$, $j = 1, 2, \ldots, m$, and $k = 1, 2, \ldots, l$. The mapping $\tilde{A}$ is then defined as follows

$$\tilde{A}(i,j) = m(i-1) + j \qquad in\ 2D \tag{11}$$

$$\tilde{A}(i,j,k) = (l \times m)(i-1) + l(j-1) + k \qquad in\ 3D \tag{12}$$

Given three knot vectors $\Xi^1 = \{\xi_1, \xi_2, \ldots \xi_{n+p+1}\}$, $\Xi^2 = \{\eta_1, \eta_2, \ldots \eta_{m+q+1}\}$, $\Xi^3 = \{\zeta_1, \zeta_2, \ldots \zeta_{l+r+1}\}$, (one for each direction), and their associate univariate B-spline basis functions $N_{i,p}(\xi)$, $M_{j,q}(\eta)$, and $L_{l,r}(\zeta)$, NURBS basis functions for surfaces and volumes are defined by the tensor product of the univariate B-spline basis functions. In two dimensions, the surface NURBS basis functions are defined as

$$R_A^{p,q}(\xi,\eta) = \frac{N_{i,p}(\xi)\, M_{j,q}(\eta)\, w_A}{\sum_{\hat{i}=1}^{n} \sum_{\hat{j}=1}^{m} N_{\hat{i},p}(\xi)\, M_{\hat{j},q}(\eta)\, w_{\hat{A}}} \tag{13}$$

where $A = \tilde{A}(i,j)$ and $\hat{A} = \tilde{A}(\hat{i},\hat{j})$. In three dimensions, the volume NURBS basis functions are defined as

$$R_A^{p,q,r}(\xi,\eta,\zeta) = \frac{N_{i,p}(\xi)\, M_{j,q}(\eta)\, L_{k,r}(\zeta)\, w_A}{\sum_{\hat{i}=1}^{n} \sum_{\hat{j}=1}^{m} \sum_{\hat{k}=1}^{l} N_{\hat{i},p}(\xi)\, M_{\hat{j},q}(\eta)\, L_{\hat{k},r}(\zeta)\, w_{\hat{A}}} \tag{14}$$

Given a *control mesh* $\{\mathbf{P}_A\}$, where $A = 1, 2, \ldots., (n \times m)$ for surfaces, and $A = 1, 2, \ldots., (n \times m \times l)$ for volumes, a NURBS surface is defined as

$$\mathbf{S}(\xi, \eta) = \sum_{A=1}^{n\times m} R_A^{p,q}(\xi, \eta)\,\mathbf{P}_A \tag{15}$$

and a NURBS volume is defined as

$$\mathbf{V}(\xi, \eta, \zeta) = \sum_{A=1}^{n\times m\times l} R_A^{p,q,r}(\xi, \eta, \zeta)\,\mathbf{P}_A. \tag{16}$$

As an example, Fig. 2 shows a control net and the corresponding NURBS surface description of a torous.

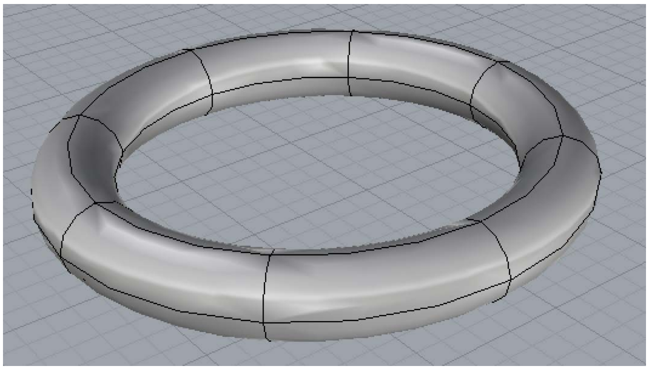

(a)

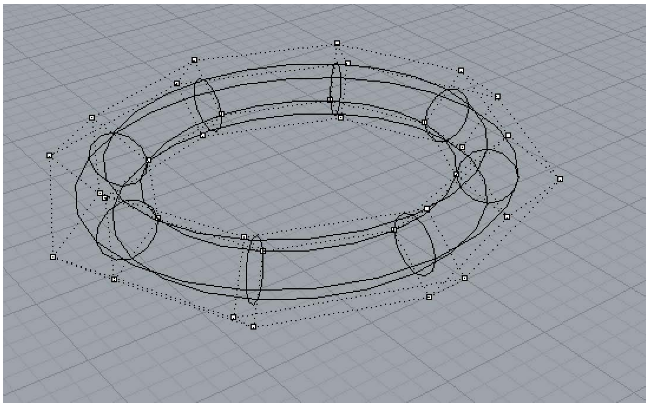

(b)

Figure 2: Toroidal geometry: (a) surface, and (b) its control net.

2.2 Limitations of NURBS-based IGA

As a design tool, a multivariate NURBS discretization, however, does not provide a natural possibility for local mesh refinement due to its rigid tensor product structure. In the context of refinement, adding new control points to a NURBS surface entails adding entire rows or columns of control points to maintain this tensor product structure This implies that:

1. A large percentage of NURBS control points contain no significant geometric information, but are only needed to satisfy topological constraints.
2. NURBS refinement is global and not local, since knot lines must extend through the entire domain.
3. Complex geometry of arbitrary genus can only be represented by multiple NURBS patches which are generally discontinuous across patch boundaries.

NURBS-based design deficiencies have a negative impact on analysis:

1. A large percentage of the Dofs are needed to satisfy topological constraints only.
2. Resolution of local features is prohibitively expensive since all refinement propagates globally. In the context of contact or debonding, global propagation of refinement is especially deleterious as the response in this case is usually a highly localized phenomena.
3. For multi-patch domains inconsistencies at patch boundaries lead to C^0 continuity at the interface or, more frequently, gaps and overlaps between patches. This lack of watertightness destroys the analysis-suitable nature of the discretization. By "analysis-suitable" (a concept mentioned several times hereafter) we mean the exact representation of the geometry due to the smooth geometric basis functions with efficient mathematical properties (i.e. partition of unity, non-negativity, convex hull property, linearly independence), whereas "smooth" refers to to the C^l interelement continuity, where $0 \le l < p$, and p is the polynomial order.

Hierarchical refinement of NURBS has recently attracted increasing attention [77, 78] due to the following advantages:

- Hierarchical B-splines rely on the principle of B-spline subdivision which makes it possible to mantain linear independence throughout the refinement process. The maximal smoothness of NURBS is maintained in a hierarchically refined basis.
- Hierarchical B-splines can be generalized to arbitrary dimensions due to their local tensor product structure nature. The simplicity of the tensor product structure automates the refinement process.
- A hierarchical organization of a basis can be directly transferred into the well-know concept of tree-like data structure [79, 80], and allows for a direct implementation with a feasible coding effort.

- Similar refinement techniques based on a hierarchical split of standard finite element bases have existed in the finite element analysis community for a long time [81-83]. This helps to increase the familiarity with hierarchical B-spline refinement.

A valid alternative in the literature for local refinement in IGA is represented by T-splines, as introduced in [69], which does not involve any notion of hierarchy: all local refinement is done on one control grid on a single hierarchical "level" and all control points have similar influence on the shape of the surface. They are an enhancement of NURBS surfaces that allow the presence of T-junction control points, and the removal of superfluous control points in a mesh. To this day, based on recent advances of IGA technology, bi-cubic T-spline surface modeling has reached sufficient maturity, for which watertight parameterizations of surfaces can be built for geometrically and topologically complex engineering designs that can be used directly as finite element meshes is structural analyses of many 3D solids, and eliminating gaps and overlaps of NURBS patches.

2.3 The unstructured T-mesh

The T-spline technology is based on the definition of a control grid named T-mesh. For surfaces, a T-mesh is a polygonal mesh and we will refer to the constituent polygons as elements or, equivalently, faces. Each element is a quadrilateral whose edges are permitted to contain T-junctions – vertices that are analogous to hanging nodes in finite elements. A control point, $\mathbf{P}_A \in \mathbb{R}^{d_s}$, $d_s = 2, 3$ and a control weight, $w_A \in \mathbb{R}$, where the index A denotes a global control point number, is assigned to each vertex in the T-mesh. The valence of a vertex is the number of edges that touch the vertex. An extraordinary point is an interior vertex that is not a T-junction and whose valence does not equal four. The spoke edges emanating from the extraordinary point are G^1 while the remaining edge interfaces of the one-ring of Bézier patches surrounding the extraordinary point are C^1 with neighboring patches. The conditions which guarantee these smoothness conditions as well as their construction in terms of Bézier extraction are detailed in [64].

When generating real world T-spline models the presence of extraordinary points in the T-mesh can not be avoided. The generation of efficient and simple element technology near extraordinary points which meet the needs of both design and analysis is crucial if IGA must be competitive with traditional finite element discretization schemes.

For T-splines, knot intervals represent the method to assign and retrieve parameter information to and from the T-mesh since no origin is required. To each vertex, A, of the T-mesh a set of *local knot interval vectors*, $\triangle\Xi_A = \left\{\Delta\Xi_A^i\right\}_{i=1}^{d_s}$ is assigned, from which the corresponding set of *local knot vectors*, $\Xi_A = \left\{\Xi_A^i\right\}_{i=1}^{d_s}$, can be derived [69].

After defining the sets of local knot vectors Ξ_A, a *local basis function domain*, $\hat{\Omega}_A \subset \mathbb{R}^{d_s}$ can be defined, over which a single T-spline basis function is identified. The local basis function domain for $d_s = 2$ is defined as follows

$$\hat{\Omega}_A = \hat{\Omega}_A^1 \otimes \hat{\Omega}_A^2 \tag{17}$$

where $\hat{\Omega}_A^i \subset \mathbb{R}$. Each local basis function domain carries a coordinate system (ξ_A, η_A), named as the basis coordinate system.

The knot coordinate system is used in writing an explicit formula for a *T-spline surface* as follows

$$\mathbf{P}(\xi,\eta) = (x(\xi,\eta), y(\xi,\eta), z(\xi,\eta), w(\xi,\eta)) = \sum_{A=1}^{n} \mathbf{P}_A N_A(\xi,\eta) \tag{18}$$

where $P_A = (x_A, y_A, z_A, w_A)$ are control points in P^4 with weights w_A, and Cartesian coordinates $\frac{1}{w_A}(x_A, y_A, z_A)$. Likewise, the Cartesian coordinates of points on the surface are given by

$$\frac{\sum_{A=1}^{n}(x_A, y_A, z_A)N_A(\xi,\eta)}{\sum_{A=1}^{n} w_A N_A(\xi,\eta)} \tag{19}$$

The *local basis functions* in eq. (18), $N_A(\xi,\eta)$, are explicitly expressed as the tensor product of the univariate basis functions as

$$N_A(\xi,\eta) = N(\xi)N(\eta) \tag{20}$$

where $N(\xi)$ and $N(\eta)$ are the cubic B-spline basis functions associated with the knot vectors Ξ_A^1 and Ξ_A^2 respectively. The univariate basis functions in eq. (20) can be rewritten in a compact way as follows

$$N_A(\xi_A \mid \Xi_A) = \prod_{i=1}^{d_s} N_A^i\left(\xi_A^i \mid \Xi_A^i\right) \tag{21}$$

The T-spline equation is very similar to the equation for a tensor-product rational B-spline surface. The difference between the T-spline equation and a B-spline equation is based on how the knot vectors Ξ_A^1 and Ξ_A^2 are determined for each blending function $N_A(\xi,\eta)$. Knot vectors Ξ_A^1 and Ξ_A^2 are inferred from the T-mesh neighborhood of $\mathbf{P}_A$, based on the rule as follows. If A is not adjacent to an extraordinary point, N_A is comprised of a 4 × 4 grid of polynomials. Otherwise, the polynomials comprising N_A do not form a 4 × 4 grid but rather an unstructured grid of polynomials.

2.4 T-splines elements

A T-spline element $\Omega^e \subset \mathbb{R}^{d_s}$ is defined as the region in the physical space which is bounded by knot lines, i.e. lines of reduced continuity in the T-spline basis. The basis functions defined in the T-spline element are C^∞. Over each element domain there exist a set of non-zero T-spline basis functions, which are in one-to-one correspondence with the T-mesh control points and are indexed by the global control point numbers. The local basis function number, a, and the element number, e, are directly mapped through the IEN array to the corresponding global control point number A. In other words $A = IEN(a, e)$. Differently from NURBS basis functions, where all the elements support exactly $(p + 1)^{d_p}$ basis functions, a variable number of T-spline basis functions can be supported by each element of the mesh. For more details, see [64].

2.5 Bézier extraction and its incorporation into the finite element formulation

In this work, T-splines from the finite element point of view are developed, utilizing Bézier extraction. The idea is to extract a linear transformation which maps the Bernstein polynomial basis on Bézier elements, to the global T-spline basis as follows

$$\mathbf{N}^e(\tilde{\boldsymbol{\xi}}) = \mathbf{C}^e\mathbf{B}(\tilde{\boldsymbol{\xi}}), \tag{22}$$

where $\tilde{\xi} \in \tilde{\Omega}$ is a coordinate in a standard Bézier parent element domain, $\mathbf{N}^e(\tilde{\xi}) = \{N_a^e(\tilde{\xi})\}_{a=1}^n$ is a vector of T-spline basis functions which are non-zero over Bézier element e, $\mathbf{B}(\tilde{\xi}) = \{B_i(\tilde{\xi})\}_{i=1}^m$ is the vector of tensor product Bernstein polynomial basis functions defining Bézier element e, and $\mathbf{C}^e \in \mathbb{R}^{n \times m}$ is the element extraction operator, defined through the coefficients, $c_{a,i}^e$, as follows

$$\mathbf{C}^e = \begin{bmatrix} c_{1,1}^e & c_{1,2}^e \cdots & c_{1,m}^e \\ c_{2,1}^e & c_{2,2}^e & c_{2,m}^e \\ \vdots & \vdots & \vdots \\ c_{n,1}^e & c_{n,2}^e & c_{n,m}^e \end{bmatrix} \tag{23}$$

Moreover, the use of the linear operator allows us to standardize the form of the element basis on the parent domain.

The transpose of the extraction operator maps the control points of the global T-spline to the control points of the Bernstein polynomials. This provides a finite element representation of T-splines, and facilitates the incorporation of T-splines into existing finite element programs. Only the shape function subroutine needs to be modified, as it has been done in our case in the FEAP code [84]. All other aspects of the finite element program remain the same. Additionally, Bézier extraction is automatic and can be applied to any T-spline regardless of topological complexity or polynomial degree. In particular, it represents an elegant treatment for T-junctions and extraordinary points.

For T-splines, the computation of the element extraction operators has been performed in [61], where each basis function contributes a row to each of the extraction operators corresponding to the Bézier elements in its support. The extraction algorithm for T-splines is based on the main steps as follows (for more details, see [61]):

- Infer the T-spline basis from the T-mesh.
- Refine the T-mesh.
- For a T-spline basis function determine the Bézier elements which are in its support.
- For a T-spline basis function perform Bézier extraction.
- The last two steps are repeated for each T-spline basis function.

The element geometric mapping, $\mathbf{X}^e : \tilde{\Omega} \to \Omega^e$, from the parent element domain onto the physical domain in the reference configuration is defined as

$$\mathbf{X}^e(\tilde{\boldsymbol{\xi}}) = \frac{1}{(\mathbf{w}^e)^T\mathbf{N}^e(\tilde{\boldsymbol{\xi}})}\left(\mathbf{P}^e\right)^T\mathbf{W}^e\mathbf{N}^e(\tilde{\boldsymbol{\xi}}) = \left(\mathbf{P}^e\right)^T\mathbf{R}^e(\tilde{\boldsymbol{\xi}}) \tag{24}$$

where $\mathbf{R}^e(\tilde{\xi}) = \{R_a^e(\tilde{\xi})\}_{a=1}^n$ is a vector of rational T-spline basis functions, $\mathbf{w}^e = \{w_a^e\}_{a=1}^n$ is the element weight vector, $\mathbf{W}^e = \mathrm{diag}(\mathbf{w}^e)$ is the diagonal weight matrix, and $\mathbf{P}^e$ is a matrix of dimension $n \times d_s$ that contains the reference coordinates of the element control points. For $d_s = 3$ it is

$$\mathbf{P}^e = \begin{bmatrix} X_1^e & Y_1^e & Z_1^e \\ X_2^e & Y_2^e & Z_2^e \\ \vdots & \vdots & \vdots \\ X_n^e & Y_n^e & Z_n^e \end{bmatrix} \tag{25}$$

Using (24) we have that

$$\mathbf{R}^e(\tilde{\boldsymbol{\xi}}) = \frac{1}{(\mathbf{w}^e)^T\mathbf{N}^e(\tilde{\boldsymbol{\xi}})}\mathbf{W}^e\mathbf{N}^e(\tilde{\boldsymbol{\xi}}) \tag{26}$$

and using (22)

$$\mathbf{R}^e(\tilde{\boldsymbol{\xi}}) = \frac{1}{(\mathbf{w}^e)^T\mathbf{C}^e\mathbf{B}(\tilde{\boldsymbol{\xi}})}\mathbf{W}^e\mathbf{C}^e\mathbf{B}(\tilde{\boldsymbol{\xi}}) \tag{27}$$

Note that all quantities in (27) are written in terms of the Bernstein basis defined over the parent element domain, $\tilde{\Omega}$.

Adopting the isoparametric approach, element mappings analogous to eq. (24) are introduced for the unknown displacement field, its variation, and the coordinates in the current configuration

$$\mathbf{u}(\tilde{\boldsymbol{\xi}}) = \sum_{a=1}^{n} R_a(\tilde{\boldsymbol{\xi}})\mathbf{u}_a \qquad \delta\mathbf{u}(\tilde{\boldsymbol{\xi}}) = \sum_{a=1}^{n} R_a(\tilde{\boldsymbol{\xi}})\delta\mathbf{u}_a$$

$$\mathbf{x}(\tilde{\boldsymbol{\xi}}) = \sum_{a=1}^{n} R_a(\tilde{\boldsymbol{\xi}})\mathbf{p}_a \tag{28}$$

where the superscript e has been dropped for convenience and $\mathbf{u}_a$, $\delta\mathbf{u}_a$ and $\mathbf{p}_a$ are, respectively, the unknown displacement, the displacement variation, and the current coordinate of the control point $\mathbf{P}_A$, with $A = IEN(a, e)$. Note that $\mathbf{p}_a = \mathbf{P}_a + \mathbf{u}_a$.

3 Large deformation frictionless contact and cohesive debonding algorithm

3.1 Problem description

Assume two hyperelastic bodies undergoing finite deformations including contact. One of them is denoted as slave body, $\mathcal{B}^s$, and the other one is the master body, $\mathcal{B}^m$ (Fig. 3a). The deformation of both bodies is expressed by the coordinates of their generic point in the current configuration $\mathbf{x}^i = \mathbf{X}^i + \mathbf{u}^i$, where $\mathbf{X}$ is the coordinate of the generic point in the reference configuration, $\mathbf{u}$ is the displacement of the same point, and the superscript $i = (s, m)$ refers to the slave and master bodies, respectively. Once the bulk parameterization is established, the parameterization of the contact surface follows immediately by fixing the value of the appropriate parametric coordinate. In this work, we assume that the third parametric coordinate takes a constant value on the contact surface.

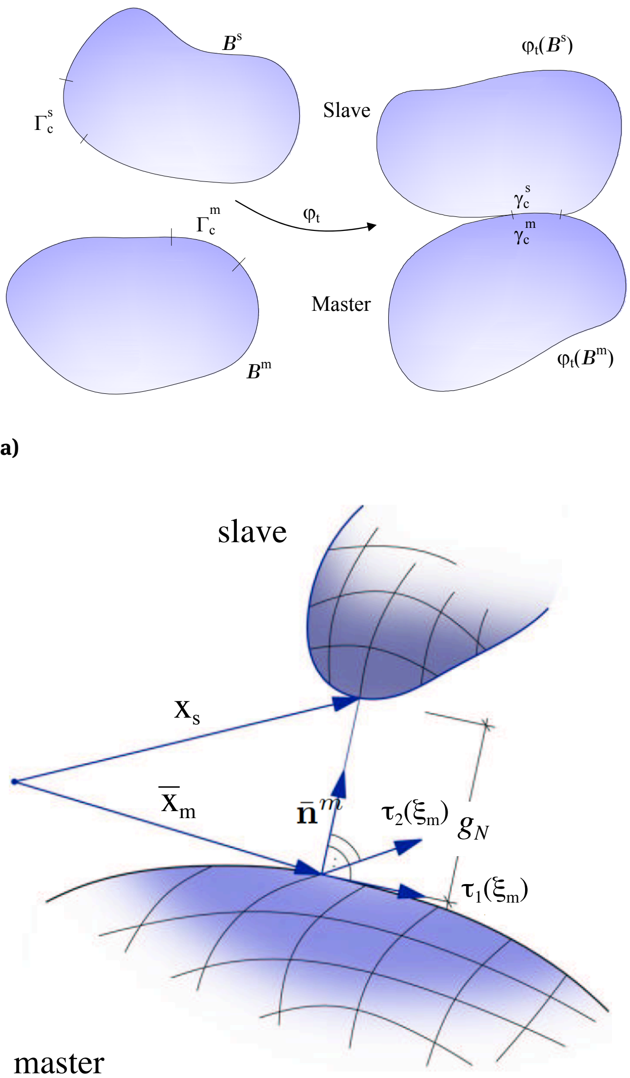

Figure 3: Geometrical variables for the contact formulation.

On the master surface, the convective coordinates $\xi_m = \{\xi_m^\alpha\}_{\alpha=1}^{d_s-1}$ are chosen coincident with the parametric coordinates of the surface and define the covariant vectors $\tau_\alpha = \mathbf{x}^m_{,\alpha}$. In order to determine the unknown contact interface in the current configuration, γ_c, we introduce the distance function $d := \|\mathbf{x}^s - \mathbf{x}^m(\xi_m)\|$, describing the distance between a fixed point $\mathbf{x}^s$ on the contact boundary γ_c^s of the slave surface and an arbitrary point $\mathbf{x}^m = \mathbf{x}^m(\xi_m)$ on the contact boundary of the master surface γ_c^m. Based on the assumption of perfect contact $\gamma_c = \gamma_c^s = \gamma_c^m$, each point $\mathbf{x}^s$ has a unique contact partner $\bar{\mathbf{x}}^m = \mathbf{x}^m(\bar{\xi}_m)$ whose position is computed via the closest-point projection of $\mathbf{x}^s$ onto γ_c^m (Fig. 3a). This is equivalent to minimizing the distance d previously defined. The residual of this closest-point projection reads

$$f_\alpha(\bar{\xi}_m) = \boldsymbol{\tau}_\alpha(\xi_m) \cdot \left[\mathbf{x}^s - \bar{\mathbf{x}}^m\right] \tag{29}$$

that vanishes at the projection point, i.e. $f_\alpha(\bar{\xi}_m) = 0$ for $\alpha = 1 \ldots (d_s - 1)$ (Fig. 3b). In the following, for simplicity of notation the bar will be omitted, and all the quantities related to the master surface will be implicitly intended as evaluated at the projection point.

The contact interface is pulled back to $\Gamma_c := \Gamma_c^s \neq \Gamma_c^m$, where Γ_c^i is the contact boundary of body $\mathcal{B}^i$ in the reference configuration. Hereafter, the contact integrals will be evaluated on Γ_c^s to facilitate the subsequent linearization.

The normal gap, g_N, between the two bodies is defined as

$$g_N = \left(\mathbf{x}^s - \mathbf{x}^m\right) \cdot \mathbf{n} \tag{30}$$

where $\mathbf{n} = \bar{\mathbf{n}}^m$ is the outward normal unit vector to the master surface. Based on this definition, g_N is positive if contact is open and negative in case of penetration between the bodies. The normal contact traction p_N is defined as the normal component of the Piola traction vector $\mathbf{t} = \mathbf{t}^m = -\mathbf{t}^s$

$$\mathbf{t} = p_N \mathbf{n} \qquad p_N = \mathbf{t} \cdot \mathbf{n} \tag{31}$$

The non-penetration condition is here enforced in the normal direction using the penalty method. Depending on the gap status, an automatic switching procedure is used to choose between contact and cohesive models. In the latter case a bilinear CZ law is considered (Fig. 4). This simple shape is able to capture the main characteristic parameters of the interface, i.e. the cohesive strength, p_{Nmax}, the ultimate value of the normal relative displacement, g_{Nu}, as well as the linear-elastic stiffness (slope of the curve in the ascending branch, $\frac{p_{Nmax}}{g_{Nmax}}$, where g_{Nmax} is the normal relative displacement at peak cohesive stress). Thus the interface law reads

$$p_N = \begin{cases} \varepsilon_N g_N & \text{for} \quad g_N < 0 \\ \frac{p_{Nmax}}{g_{Nmax}} g_N & \text{for} \quad 0 \le g_N < g_{Nmax} \\ p_{Nmax} \frac{g_{Nu} - g_N}{g_{Nu} - g_{Nmax}} & \text{for} \quad g_{Nmax} \le g_N < g_{Nu} \\ 0 & \text{for} \quad g_N \ge g_{Nu} \end{cases} \tag{32}$$

where $\varepsilon_N > 0$ is the normal penalty parameter. The non-penetration condition in compression is enforced exactly in the limit as ε_N tends to infinity.

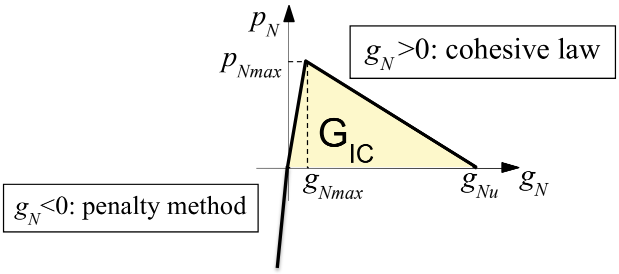

Figure 4: Relationship between interfacial tractions and relative displacements in the normal direction.

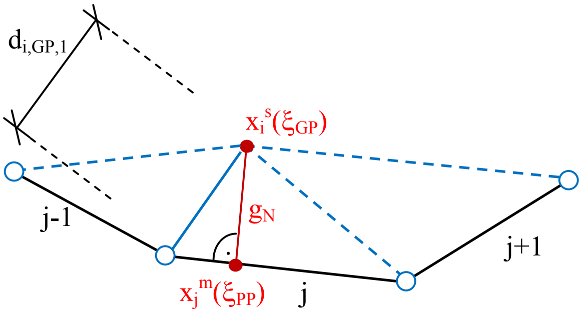

Figure 5: Find the closest master control point and correct facet.

The variation and the linearization of the normal gap are now introduced, for details see [85, 86]

$$\delta g_N = \left(\delta \mathbf{x}^s - \delta \mathbf{x}^m\right) \cdot \mathbf{n} \tag{33}$$

$$\Delta\left(\delta g_N\right) = -\left(\delta \mathbf{x}^m_{,\alpha} \Delta \xi^\alpha_m + \Delta \mathbf{x}^m_{,\alpha} \delta \xi^\alpha_m\right) \cdot \mathbf{n} - \delta \xi^\alpha_m k_{\alpha\beta} \Delta \xi^\beta_m + g_N \delta \mathbf{n} \cdot \Delta \mathbf{n} \tag{34}$$

where

$$\delta \mathbf{n} = -\left(\delta \mathbf{x}^m_{,\alpha} \cdot \mathbf{n} + k_{\alpha\beta} \delta \xi^\beta_m\right) \tau^\alpha \tag{35}$$

and

$$\delta \xi^\beta_m = A^{\alpha\beta} \left[\left(\delta \mathbf{x}^s - \delta \mathbf{x}^m\right) \cdot \tau_\alpha + g_N \mathbf{n} \cdot \delta \mathbf{x}_{,\alpha}{}^m\right] \tag{36}$$

In the previous equations, $k_{\alpha\beta} = \mathbf{x}^m_{\alpha,\beta} \cdot \mathbf{n}$ is the symmetric curvature tensor and $\tau^\alpha := m^{\alpha\beta} \tau_\beta$ are the contravariant vectors, with $m^{\alpha\beta}$ as the inverse components of the metric tensor $m_{\alpha\beta} := \tau_\alpha \cdot \tau_\beta$. Moreover, $A^{\alpha\beta}$ in eq. (36) are the inverse components of

$$A_{\alpha\beta} = m_{\alpha\beta} - g_N k_{\alpha\beta} \tag{37}$$

and $\beta = 1 \ldots (d_s - 1)$.

In the same manner, the linearized increments Δg_N, $\Delta \mathbf{n}$, $\Delta \xi^\beta_m$ are obtained as in the following

$$\Delta g_N = \left(\Delta \mathbf{x}^s - \Delta \mathbf{x}^m\right) \cdot \mathbf{n} \tag{38}$$

$$\Delta \mathbf{n} = -\left(\Delta \mathbf{x}^m_{,\alpha} \cdot \mathbf{n} + k_{\alpha\beta} \Delta \xi^\beta_m\right) \tau^\alpha \tag{39}$$

$$\Delta \xi^\beta_m = A^{\alpha\beta} \left[\left(\Delta \mathbf{x}^s - \Delta \mathbf{x}^m\right) \cdot \tau_\alpha + g_N \mathbf{n} \cdot \Delta \mathbf{x}_{,\alpha}{}^m\right]. \tag{40}$$

3.2 Contact virtual work

The frictionless contact problem can be formulated as the constrained minimization of the potential energy W.

Based on the penalty regularization, the frictionless contact contribution to the virtual work follows as

$$\delta W_c = \int_{\Gamma_c} p_N \delta g_N \, d\Gamma \tag{41}$$

where the integral is evaluated on the currently active contact region by means of an active set strategy.
Linearization of eq. (41) yields

$$\triangle \delta W_c = \int_{\Gamma_c} \frac{\partial p_N}{\partial g_N} \triangle g_N \delta g_N d\Gamma + \int_{\Gamma_c} p_N \Delta\left(\delta g_N\right) d\Gamma \tag{42}$$

where

$$\frac{\partial p_N}{\partial g_N} = \begin{cases} \varepsilon_N & \text{for} \quad g_N \leq 0 \\ \frac{p_{Nmax}}{g_{Nmax}} & \text{for} \quad 0 < g_N < g_{Nmax} \\ -\frac{p_{Nmax}}{g_{Nu} - g_{Nmax}} & \text{for} \quad g_{Nmax} < g_N \leq g_{Nu} \\ 0 & \text{for} \quad g_N > g_{Nu} \end{cases} \tag{43}$$

3.3 Geometrical approach

The computation of frictionless contact problems must deal with the relative movement between the contact surfaces. Therefore the point of projection ξ_m has to be updated within the iterative solution procedure because it is not fixed. Locating the actual position of ξ_m within the global solution algorithm results from an iterative update which has to be performed before solving the global equation system. This is due to the fact that ξ_s has to be known before the discrete contact problem can be formulated because it contributes to the contact virtual work. The update is based on the condition of the minimal distance check between x^s and x^m each time. The associated constraint is already given by the condition $f_\alpha(\xi_m) = 0$ as previously mentioned.

Within the iterative solution procedure the nonlinear mechanical contact problem is solved in such a way that the load is applied in time steps. This means that the mechanical system is loaded up not until the system is in equilibrium with the load at a given time step t_n. Then a new load increment is applied such that after balancing the system within the time increment $\triangle t_{n+1} = t_{n+1} - t_n$ a new deformation state is solved for the actual time step t_{n+1} . The incremental update of ξ_m within a time step is done by using the Newton's method, as shown in Table 1.

Table 1: Contact search for projection points.

```
Initialization: $i = 0$, $\xi_{i,m} = \bar{\xi}_n$ (last converged posistion)
LOOP over NETWON iterations: i=1,...convergence
    Compute:
    $f_\alpha(\xi_{i,m}) = [\mathbf{x}^s - \mathbf{x}_i^m] \cdot \boldsymbol{\tau}_\alpha(\xi_{i,m}) = 0$
    Check for convergence: IF $f_\alpha(\xi_{i,m}) \leq TOL \Rightarrow STOP\ AND\ SET\ \bar{\xi}_{n+1} = \xi_{i,m}$
    Compute:
    $f_{\alpha,\xi}(\xi_{i,m}) = - \parallel \boldsymbol{\tau}_\alpha(\xi_{i,m}) \parallel^2 + (\mathbf{x}^s - \mathbf{x}_i^m) \cdot \mathbf{x}_{i,\xi\xi}^m$
    Complete NETWON step:
    $\xi_{i+1,m} = \xi_{i,m} - \frac{f_\alpha(\xi_{i,m})}{f_{\alpha,\xi}(\xi_{i,m})}$, set $\xi_i = \xi_{i+1}$
END LOOP
```

3.4 Variation and linearization of the contact variables in discretized form

The quantities δg_N, Δg_N and $\Delta\left(\delta g_N\right)$ needed in eqs. (41) and (42) can be rewritten in matrix form by introducing the T-spline interpolations (28) into eqs. (33) and (34). The following results are obtained

$$\delta g_N = \delta \mathbf{u}^T \mathbf{N} \qquad \triangle g_N = \mathbf{N}^T \triangle \mathbf{u} \tag{44}$$

$$\begin{aligned} \triangle \delta g_N = \delta \mathbf{u}^T \{ & g_N \left[m^{11} \overline{\mathbf{N}}_1 \overline{\mathbf{N}}_1^T + m^{12} \left(\overline{\mathbf{N}}_1 \overline{\mathbf{N}}_2^T + \overline{\mathbf{N}}_2 \overline{\mathbf{N}}_1^T \right) + m^{22} \overline{\mathbf{N}}_2 \overline{\mathbf{N}}_2^T \right] \\ & + \mathbf{D}_1 \mathbf{N}_1^T + \mathbf{D}_2 \mathbf{N}_2^T + \mathbf{N}_1 \mathbf{D}_1^T + \mathbf{N}_2 \mathbf{D}_2^T - k_{11} \mathbf{D}_1 \mathbf{D}_1^T - k_{22} \mathbf{D}_2 \mathbf{D}_2^T \\ & - k_{12} \left(\mathbf{D}_1 \mathbf{D}_2^T + \mathbf{D}_2 \mathbf{D}_1^T \right) \} \Delta \mathbf{u} \end{aligned} \tag{45}$$

where

$$\delta \mathbf{u} = \begin{bmatrix} \delta \mathbf{u}_1^s \\ \vdots \\ \delta \mathbf{u}_{n^s}^s \\ \delta \mathbf{u}_1^m \\ \vdots \\ \delta \mathbf{u}_{n^m}^m \end{bmatrix} \qquad \triangle \mathbf{u} = \begin{bmatrix} \triangle \mathbf{u}_1^s \\ \vdots \\ \triangle \mathbf{u}_{n^s}^s \\ \triangle \mathbf{u}_1^m \\ \vdots \\ \triangle \mathbf{u}_{n^m}^m \end{bmatrix} \tag{46}$$

$$\mathbf{N} = \begin{bmatrix} R_1^s(\xi_s^1, \xi_s^2)\mathbf{n} \\ \vdots \\ R_{n^s}^s(\xi_s^1, \xi_s^2)\mathbf{n} \\ -R_1^m(\bar{\xi}^1, \bar{\xi}^2)\mathbf{n} \\ \vdots \\ -R_{n^m}^m(\bar{\xi}^1, \bar{\xi}^2)\mathbf{n} \end{bmatrix} \qquad \mathbf{T}_\alpha = \begin{bmatrix} R_1^s(\xi_s^1, \xi_s^2)\boldsymbol{\tau}_\alpha \\ \vdots \\ R_{n^s}^s(\xi_s^1, \xi_s^2)\boldsymbol{\tau}_\alpha \\ -R_1^m(\bar{\xi}^1, \bar{\xi}^2)\boldsymbol{\tau}_\alpha \\ \vdots \\ -R_{n^m}^m(\bar{\xi}^1, \bar{\xi}^2)\boldsymbol{\tau}_\alpha \end{bmatrix}$$

$$\mathbf{N}_\alpha = \begin{bmatrix} 0 \\ \vdots \\ 0 \\ -R_{1,\alpha}^m(\bar{\xi}^1, \bar{\xi}^2)\mathbf{n} \\ \vdots \\ -R_{n^m,\alpha}^m(\bar{\xi}^1, \bar{\xi}^2)\mathbf{n} \end{bmatrix} \tag{47}$$

$$\mathbf{D}_1 = \frac{1}{det[\mathbf{A}]}\left[A_{22}\left(\mathbf{T}_1 - g_N\mathbf{N}_1\right) - A_{12}\left(\mathbf{T}_2 - g_N\mathbf{N}_2\right)\right] \tag{48}$$

$$\mathbf{D}_2 = \frac{1}{det[\mathbf{A}]}\left[A_{11}\left(\mathbf{T}_2 - g_N\mathbf{N}_2\right) - A_{12}\left(\mathbf{T}_1 - g_N\mathbf{N}_1\right)\right] \tag{49}$$

$$\overline{\mathbf{N}}_1 = \mathbf{N}_1 - k_{11}\mathbf{D}_1 - k_{12}\mathbf{D}_2 \qquad \overline{\mathbf{N}}_2 = \mathbf{N}_2 - k_{12}\mathbf{D}_1 - k_{22}\mathbf{D}_2 \tag{50}$$

In the above equations, n^s and n^m are the number of basis functions having support on the element of the slave and master body, respectively, where the quantities are currently being evaluated; (ξ_s^1, ξ_s^2) are the parametric coordinates of the point on the slave surface where the quantities are being evaluated, and $(\bar{\xi}^1, \bar{\xi}^2)$ are the parametric coordinates of the respective projection point on the master surface. A similar vectorial notation for the above geometrical quantities is adopted in [85, 86] for Lagrange polynomials, and [16, 17] for NURBS discretizations. In both cases, the size of all vectors is fixed and dictated by the order of the discretization. Conversely, in the present case the above vectors have variable size depending on the number of basis functions having support on each given slave or master element, which is dictated not only by the polynomial order but also by the presence and number of T-junctions and extraordinary points.

3.5 The Gauss-point-to-surface (GPTS) algorithm

The formulation adopted herein was first proposed in [25], and later extended to NURBS discretizations in [13, 16]. This contact formulation is herein denoted as Gauss-point-to-surface (GPTS), since it is characterized by the independent enforcement of the contact constraints at each quadrature point associated with the contribution δW_c in eq. (41). In other words, the contact contribution to the virtual work δW_c in eq. (41) is integrated in a straightforward fashion by locating a predetermined number of Gauss-Legendre quadrature points on each element of the slave contact surface. Computation of the integral is combined with an active set strategy, so that only the contributions of quadrature points with negative values of the gap g_N are included.

The GPTS algorithm has been chosen in this investigation due to its remarkable simplicity of formulation and implementation. Compared to more sophisticated mortar-based approaches, the algorithm is also computationally inexpensive as it does not require the computation nor the storage of quantities such as the mortar integrals [13, 16, 87]. Also, the GPTS formulation was shown in [25] to pass (up to within the integration error) the so-called contact patch test [2, 88], which is a necessary condition for convergence to the correct solution for contact problems with non-matching meshes in the contacting bodies. The only disadvantage of the formulation is its overconstrained nature, due (loosely speaking) to the enforcement of the contact constraints at an “excessive” number of locations. This leads to Ladyzenskaja-Babuška-Brezzi (LBB) instability whenever the contact constraints are enforced exactly or nearly exactly, i.e., when using the Lagrange multiplier or augmented Lagrange multiplier methods, or when using the penalty method with very large values of the penalty parameter. Oscillatory responses from the GPTS formulation with very large ε_N were demonstrated in [13, 16]. Moreover, while LBB stability is a desirable feature for a contact algorithm, the values of the penalty parameter for which the drawbacks of instability become appreciable for the GPTS algorithm seem to lay beyond those needed for a solution of satisfactory quality from the engineering perspective, and in a range where issues related to ill-conditioning of the global stiffness matrix may also arise. Thus, in our experience the proposed formulation in combination with the penalty method always delivers satisfactory results, and does not place appreciable limitations on the value of the penalty parameter in addition to those stemming from ill-conditioning issues.

3.6 Solution algorithm

In large deformation contact problems the active contact surface can change its position and size. One of the most

important things is to identify and update the active set in a fast and accurate manner. The update is computationally expensive considering the numerical cost of engineering applications with many Dofs where a large number of surfaces exists which can come in contact with different other surfaces. The whole potential contact area must be checked permanently if contact constraints equal an active (inactive) status or remain active (inactive). For this reason the generalized contact search can dominate the computational time such that an efficient contact detection method is essential to reduce the computational cost.
The contact check is basically divided into two parts:

- Search for all potential contact pairings
  - to detect point-wise pairings $(\mathbf{x}^s, \mathbf{x}^m)$
  - to consider the change of contact pairings due to the change of ξ_{GP}, where ξ_{GP} is the parametric coordinate of each Gauss point
- Detection of active contact pairings
  - to activate/inactivate contact constraints for each pairing

For an active contact, the contact stiffness and residual contributiona are computed.

Search for potential contact pairings

Within the described contact search, the locating of potential contact pairings includes a global search where, for each predefined position vector $\mathbf{x}^s_i(\xi_{GP})$ in a slave facet i, the closest point projection $\mathbf{x}^m_j(\xi_{PP})$ on the master facet j must be determined. Hence the master facet j must be searched out and afterwards within this facet the coordinate ξ_{PP} can be derived by fulfilling the minimal distance. The associated search algorithm is depicted in Table 2 (see Fig. 5).
Herein, the correct master facet j with respect to the slave facet i is determined by locating the closest master control point first. Therefore, the minimal distances between $\mathbf{x}^s_i(\xi_{GP})$ and all first local control point position vectors $\mathbf{x}^m_{j1}$ are compared (Fig. 5).

Table 2: Contact search for potential pairings.

```
LOOP over all slave facets $Fs : i = 1, \ldots, Fs$
    LOOP over all GAUSS points $Ng : GP = 1, \ldots, Ng$
        LOOP over all master facets $Fm : j = 1, \ldots, Fm$
            Find $\mathbf{x}^m_{j1} \in \Gamma_{c_i}$ which minimizes $d_{i,GP,1} = \| \mathbf{x}^s_i(\xi_{GP}) - \mathbf{x}^m_{j1} \|$
            Find $\xi_{GP} \in \Gamma_{c_{i-1}}$ which fulfills $(\mathbf{x}^s_i(\xi_{GP}) - \mathbf{x}^m_{j-1}(\xi_{PP})) \cdot \boldsymbol{\tau}_\alpha(\xi_{PP}) = 0$
            Compute $d_{i,GP,j-1} = \| \mathbf{x}^s_i(\xi_{GP}) - \mathbf{x}^m_{j-1}(\xi_{PP}) \|$ and set $\xi_{PP,j-1} = \xi_{PP}$
            Find $\xi_{GP} \in \Gamma_{c_i}$ which fulfills $(\mathbf{x}^s_i(\xi_{GP}) - \mathbf{x}^m_j(\xi_{PP})) \cdot \boldsymbol{\tau}_\alpha(\xi_{PP}) = 0$
            Compute $d_{i,GP,j} = \| \mathbf{x}^s_i(\xi_{GP}) - \mathbf{x}^m_j(\xi_{PP}) \|$ and set $\xi_{PP,j-1} = \xi_{PP}$
            Compute $g_N = min(d_{i,GP,j-1}, d_{i,GP,j})$
            $\Rightarrow$ Potential contact pairing: $\mathbf{x}^s(\xi_{GP})$,$\mathbf{x}^m(\xi_{PP})$
        END LOOP over all master facets
    END LOOP over all GAUSS points
END LOOP over all slave facets
```

Detection of active contact pairings

The active contact surface follows the following conditions

$$\begin{array}{c} 0 < g_N \le g_{Nu} \rightarrow \mathit{separation} \ \Leftrightarrow p_N > 0 \rightarrow \ \mathit{Active\ GP} \\ \mathit{within\ a\ master\ facet\ for\ debonding} \\ g_N \le 0 \rightarrow \mathit{perfect\ contact} \Leftrightarrow p_N < 0 \rightarrow \ \mathit{Active\ GP\ within} \\ \mathit{a\ master\ facet\ for\ compression} \end{array} \tag{51}$$

The associated algorithm is summarized in Table 3.

Table 3: GPTS Algorithm for detection of active contact pairings.

```
LOOP over all slave facets $Fs : i = 1, \dots, Fs$
  LOOP over all potential GAUSS points parings $Ng : GP = 1, \dots, Ng$
    IF $gN \leq 0$ ⇒pairing GP active for contact ⇒compute the compressive contact contribution of $\mathbf{R}$ and $\mathbf{K}_T$
      IF $0 < gN \leq gNu$ ⇒pairing GP active for debonding ⇒compute the debonding contribution of $\mathbf{R}$ and $\mathbf{K}_T$
      ELSE pairing GP is not active ⇒the contact contribution of $\mathbf{R}$ and $\mathbf{K}_T$ is equal to zero
      END IF
    END IF
  END LOOP over all potential GAUSS points parings
END LOOP over all slave facets
```

Contact stiffness and residual contribution

By substitution of eq. (44) into eq. (41), the contact contribution to the residual vector for the Newton-Raphson iterative solution of the non-linear problem is obtained as follows

$$\mathbf{R} = \int_{\Gamma_c} p_N \mathbf{N} d\Gamma \tag{52}$$

which is numerically computed on Γ_c as

$$\mathbf{R} = \sum_{GP,active} p_{Ng} \mathbf{N}_g w_g j_g \tag{53}$$

where the subscript g indicates that the quantity is computed at the g^{th} GP on Γ_c, w_g and j_g are respectively the weight and the jacobian associated to the same Gauss point, and the summation is extended to all GPs in contact. From eq. (42) combined with eqs. (44) and (45) the expression of the consistent tangent stiffness matrix results as

$$\mathbf{K}_T = \mathbf{K}_{T,main} + \mathbf{K}_{T,geo} \tag{54}$$

where the "main" and "geometric" components are given by

$$\mathbf{K}_{T,main} = \int_{\Gamma_c} \frac{\partial p_N}{\partial g_N} \mathbf{N}\mathbf{N}^T d\Gamma \tag{55}$$

$$\begin{aligned} \mathbf{K}_{T,geo} = \int_{\Gamma_c} p_N \{ g_N & \left[m^{11} \overline{\mathbf{N}}_1 \overline{\mathbf{N}}_1^T + m^{12} \left(\overline{\mathbf{N}}_1 \overline{\mathbf{N}}_2^T + \overline{\mathbf{N}}_2 \overline{\mathbf{N}}_1^T \right) \right. \\ & \left. + m^{22} \overline{\mathbf{N}}_2 \overline{\mathbf{N}}_2^T \right] + \mathbf{D}_1 \mathbf{N}_1^T + \mathbf{D}_2 \mathbf{N}_2^T + \mathbf{N}_1 \mathbf{D}_1^T + \mathbf{N}_2 \mathbf{D}_2^T \\ & - k_{11} \mathbf{D}_1 \mathbf{D}_1^T - k_{22} \mathbf{D}_2 \mathbf{D}_2^T - k_{12} \left(\mathbf{D}_1 \mathbf{D}_2^T + \mathbf{D}_2 \mathbf{D}_1^T \right) \} d\Gamma \end{aligned} \tag{56}$$

Finally, the numerical integration of eqs. (55) and (56) yields

$$\mathbf{K}_{T,main} = \sum_{GP,active} \left. \frac{\partial p_N}{\partial g_N} \right|_g \mathbf{N}_g \mathbf{N}_g^T w_g j_g \tag{57}$$

$$\begin{aligned} \mathbf{K}_{T,geo} = \sum_{GP,active} p_{Ng} \{ g_{N,g} & \left[m_g^{11} \overline{\mathbf{N}}_{1g} \overline{\mathbf{N}}_{1g}^T + m_g^{12} \left(\overline{\mathbf{N}}_{1g} \overline{\mathbf{N}}_{2g}^T + \overline{\mathbf{N}}_{2g} \overline{\mathbf{N}}_{1g}^T \right) \right. \\ & \left. + m_g^{22} \overline{\mathbf{N}}_{2g} \overline{\mathbf{N}}_{2g}^T \right] + \mathbf{D}_{1g} \mathbf{N}_{1g}^T + \mathbf{D}_{2g} \mathbf{N}_{2g}^T + \mathbf{N}_{1g} \mathbf{D}_{1g}^T + \mathbf{N}_{2g} \mathbf{D}_{2g}^T \\ & - k_{11g} \mathbf{D}_{1g} \mathbf{D}_{1g}^T - k_{22} \mathbf{D}_{2g} \mathbf{D}_{2g}^T - k_{12g} \left(\mathbf{D}_{1g} \mathbf{D}_{2g}^T + \mathbf{D}_{2g} \mathbf{D}_{1g}^T \right) \} w_g j_g \end{aligned} \tag{58}$$

4 Numerical examples: contact

The GPTS algorithm has been implemented in the finite element code FEAP [84] and some numerical examples have been solved to demonstrate its performance in combination with T-spline parameterizations. For comparison purposes, not only T-splines but also NURBS and Lagrange discretizations with the same number of Dofs, or equivalently with the same number of control variables (control points or nodes) are employed. The current T-spline technology only encompasses third-degree interpolations, whereas for NURBS and Lagrange interpolations different degrees are adopted. Cubic T-spline discretizations are denoted by T, while NURBS and Lagrange discretizations with order p in all parametric directions are denoted as N_p, and L_p, respectively. Lagrange and NURBS meshes are uniform, whereas in the T-spline parameterizations T-junctions are locally added to the meshes near the interfaces.

The sets of comparisons presented hereafter is intended as follows. First, Lagrange and NURBS models with the same number of Dofs are compared. Despite

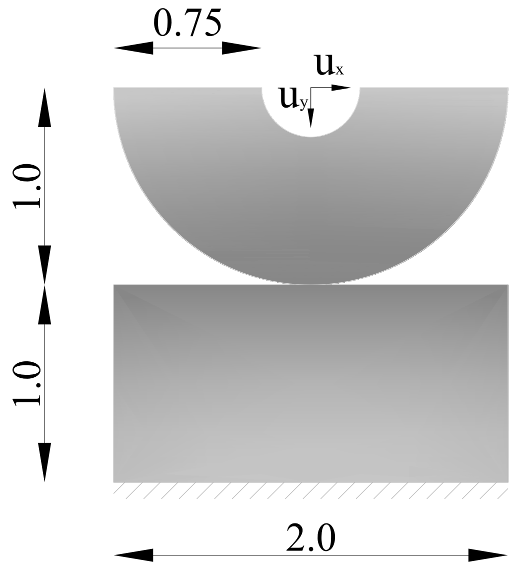

Figure 6: Ironing problem scheme.

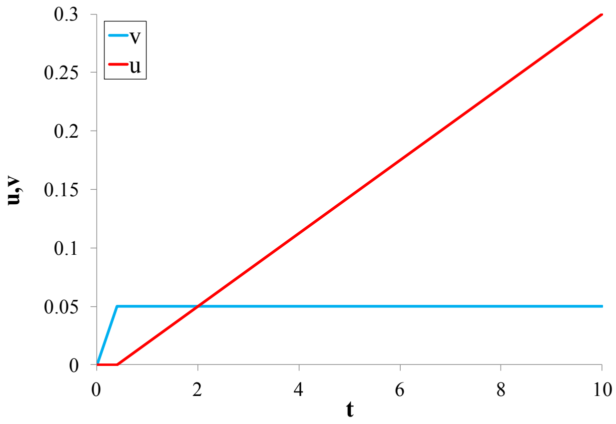

Figure 7: Loading history.

Lagrange interpolations are capable of local refinement, this possibility is not exploited here, in order for the Lagrange/NURBS comparison to focus on the effect of the different basis functions on performance. Second, NURBS and T-spline models with the same number of Dofs are compared, to quantify the increase in accuracy obtained through the local refinement capability for a given computational cost. The accuracy of NURBS for given Dofs may be improved by using non-uniform knot vectors such as done in [19]. However, this possibility is not analysed herein to avoid introducing additional variables such as the grading ratios, which are not believed to be significant for the purpose of the present investigation.

Two examples are herein presented which consider a frictionless 2D ironing problem, where contact delivers tangential motion between the deformable slave and master bodies, and a 3D application which features two semi-spheres undergoing normal contact in large deformation regime. A fixed number of 2 GPs is adopted for the evaluation of the interface integrals on each surface element in each surface parametric direction.

4.1 Ironing problem

As first example we consider a cylindrical die (treated as slave body) pressed into an elastic slab (treated as master body) and then moved in the tangential direction (Fig. 6). The lower surface of the slab is restrained in all directions. A uniform downward displacement $u_y = 0.05$ is applied to the upper line of the die in 20 time steps and then maintained constant while a horizontal dispalcment $u_x = 0.3$ is applied in a further 480 time steps (see the loading history in Fig. 7). Both bodies use a Neo-Hookean elastic material model [89]

$$\boldsymbol{\sigma} = \frac{\Lambda}{J}\left(lnJ\right)\boldsymbol{I} + \frac{\mu}{J}\left(\mathbf{F}\mathbf{F}^{T} - \mathbf{I}\right) \tag{59}$$

where J is the determinant of the deformation gradient $\mathbf{F}$ and $\mathbf{I}$ is the identity tensor. The shear modulus $\mu = E/\left(2(1+\nu)\right)$ and the bulk modulus $\Lambda = 2\mu\nu/(1-2\nu)$ are expressed in terms of Young's modulus E and Poisson's ratio ν, which are taken as $E_1 = 2$, $\nu_1 = 0.3$ for the die, and $E_2 = 1$, $\nu_2 = 0.3$ for the slab. A penalty parameter $\varepsilon_N = 10^3$ is chosen as the default value.

To investigate on the effect of the contact resolution on results, the mesh refinement is varied in the numerical analyses. The problem is solved with uniform Lagrange and NURBS meshes, as well as with locally refined T-spline meshes. Lagrange and NURBS discretizations of different orders are first considered. Then, all third-order discretizations including T-splines are compared. All comparisons are made for the same number of total Dofs. Three different levels of mesh refinement are studied, corresponding to Dof = 1044 (mesh 1), Dof = 3352 (mesh 2), and Dof = 11904 (mesh 3). Figs. 8, 9, and 10 show all the analysed meshes for Lagrange, NURBS and T-spline interpolations. Due to the possibility of local refinement through the insertion of repeated T-junctions in the initial mesh, for a given total number of Dofs, T-discretizations have a larger number of elements concentrated in the vicinity of the contact surface.

The response is evaluated in terms of the total reaction forces in the vertical (Fig. 11) and horizontal (Fig. 12) directions, computed on the top line of the die as a function of time. As visible in Figs. 11 and 12, the parameterization clearly affects the magnitude and regularity of the force os-

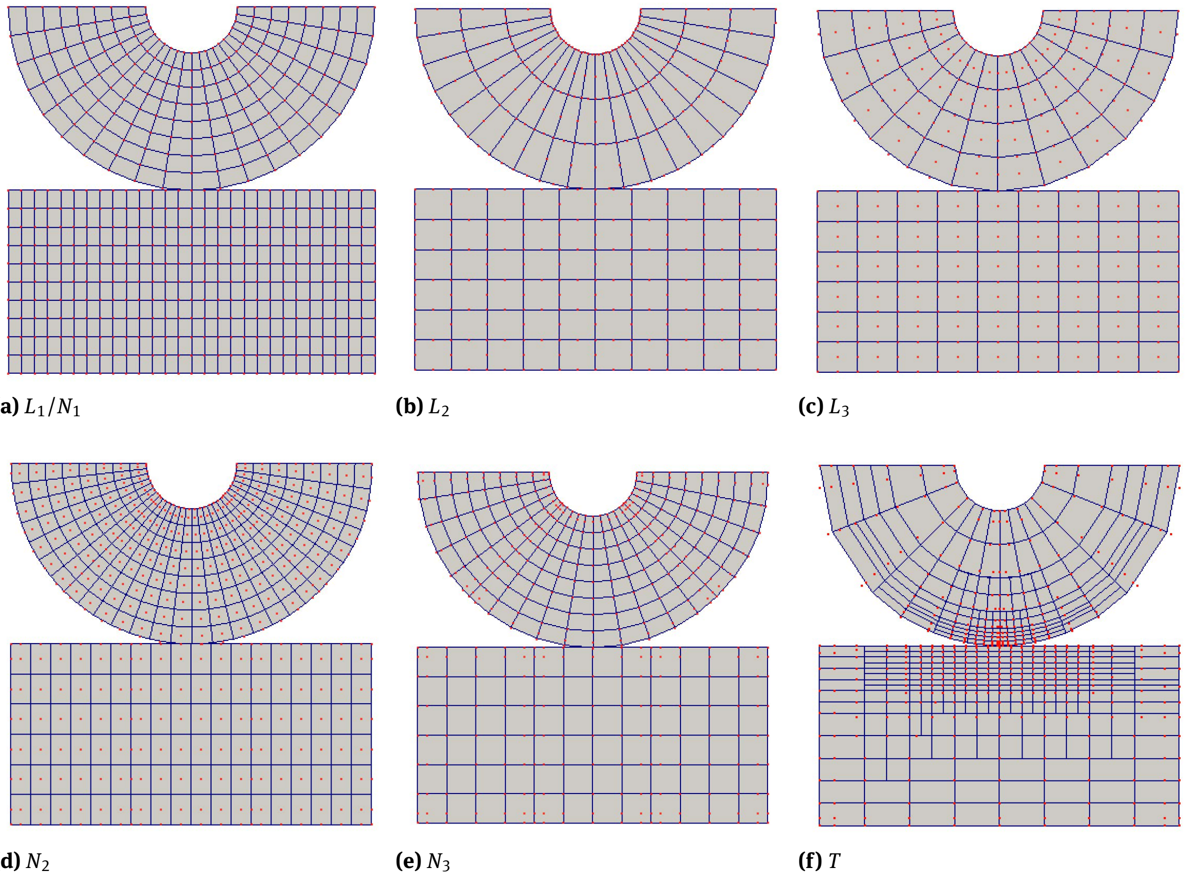

Figure 8: Ironing problem: Lagrange, NURBS, and T-spline meshes. Dof = 1044.

cillations in both directions. Lagrange interpolations yield irregular force variations which increase in the magnitude of the oscillations as the polynomial order increases, thus worsening the iterative convergence performace. For Lagrange discretizations, the third-order case gives in any case the worst results in both directions. Using the second-order NURBS discretization greatly improves the quality of results, as visible from the more regular pattern of the curves. This is due to the higher inter-element continuity in the discretization of both the bulk and the contact surface. The results monotonically improve for increasing orders of the NURBS interpolation. These results qualitatively resemble those presented in [13, 16, 17] for unilateral contact problems. The same curves obtained with T-splines, in any case, feature the smallest oscillations in comparison with those from NURBS-based interpolations with the same Dofs, as a direct consequence of the locally refined contact zone.

As the mesh is refined, the contact region is better resolved and the quality of the solution improves, as visible by comparing all the curves for each discretization in the close-up views of Fig. 11 (for the vertical responses), as well as in Fig. 12 (for the horizontal responses). A quantitative evaluation of the oscillation magnitude is also measured for each parameterization as the difference between the maximum and the minimum reaction forces P_y, and P_x, in the vertical and horizontal direction, respectively. In other words, $\triangle P_x = max(P_x) - min(P_x)$, $\triangle P_y = max(P_y) - min(P_y)$. As shown in Figs. 13, the rate of convergence varies for the three types of discretization and polynomial order, while remaining almost the same when $L3$, $N3$ and T discretizations are comparatively assessed because of the same polynomial order. The T-spline curves of Figs. 13(a)-(d), however, lie always below the NURBS curves, which in turn are lower than the Lagrange ones for the same Dofs. Anyway, the T-spline refinement performed in this work is not guided by error estimation procedures. Therefore the convergence rate achieved for T-splines may not be optimal, and possibly improve by applying adaptive local refinements. Fig. 14 finally shows the deformed mesh for the coarsest T-spline discretization at different time steps, along with the contours of the σ_y stresses.

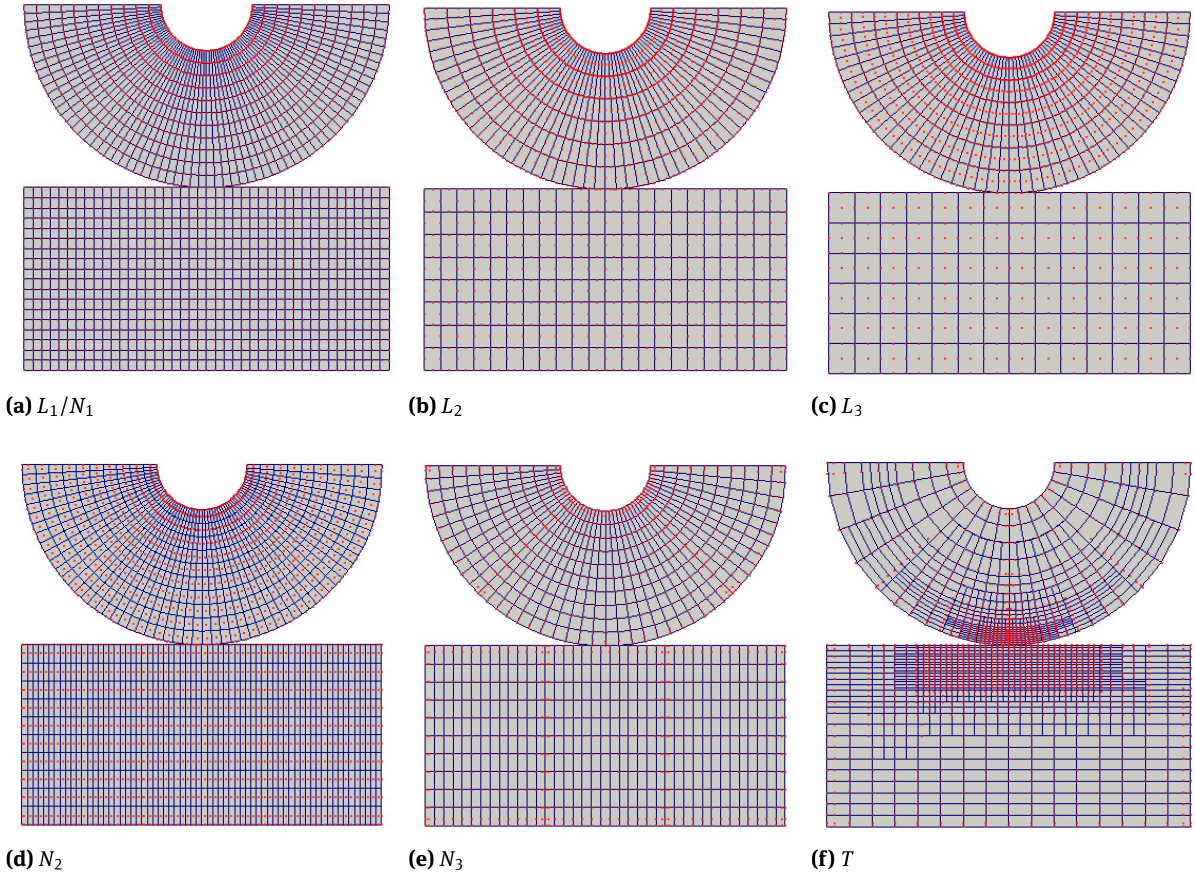
(a) L_1/N_1 (b) L_2 (c) L_3

(d) N_2 (e) N_3 (f) T

Figure 9: Ironing problem: Lagrange, NURBS, and T-spline meshes. Dof = 3352.

4.2 Hemispheres in sliding contact

The second example features two 3D hemispheres undergoing normal contact in large deformation in order to demonstrate the effectiveness of the proposed formulation in conjunction with 3D T-spline discretizations using isogeometric Kirchoff-Love shell elements for the continuum [90]. Some irregular elements are herein generated in the discretization by including extraordinary points with valence 3 in the T-mesh. Also in this case, the analysis is carried out by importing into FEAP the extraction operator generated by the T-spline plugin in the Rhino environment, where the mesh is generated using standard CAD operations.

An elastic isotropic behavior is assumed for both bodies, with material properties $E = 10^3$ and $\nu = 0.3$. The lower body, here treated as master, is held fixed at the bottom edges, and a uniform vertical displacement $U_z = -0.2$ is applied to the upper surface of the slave (upper) body in 15 time steps. The penalty parameter is $\varepsilon_N = 10^4$. Figs. 15, 16, and 17 depict snapshots for the 5th, 10th and the last time steps, respectively, from the time-history response of the simulated bodies, including the in-plane displacement contours U_x (Figs. 15a,b; 16a,b; 17a,b) and U_y (Figs. 15c,d; 16c,d; and 17c,d) as well as the downward displacement contour U_z (Figs. 15e,f; 16e,f; and 17e,f). The global contact interactions are monitored through the time variation of the total normal forces applied to the upper body, as shown in Fig. 18. Smooth force vs. time responses are observed despite the relative coarseness of the mesh, as well-resolved deformed contact interfaces with smooth transitions between adjacent elements are guaranteed by the C^2-continuous T-splines.

5 Numerical examples: debonding

As demonstration of the capabilities of T-spline-based IGA discretizations in the context of debonding, we present some numerical applications of bilinear CZ models for challenging mode-I debonding problems where local softening in the interface elements of cohesive cracks can result in a sudden release of the elastic strain energy stored

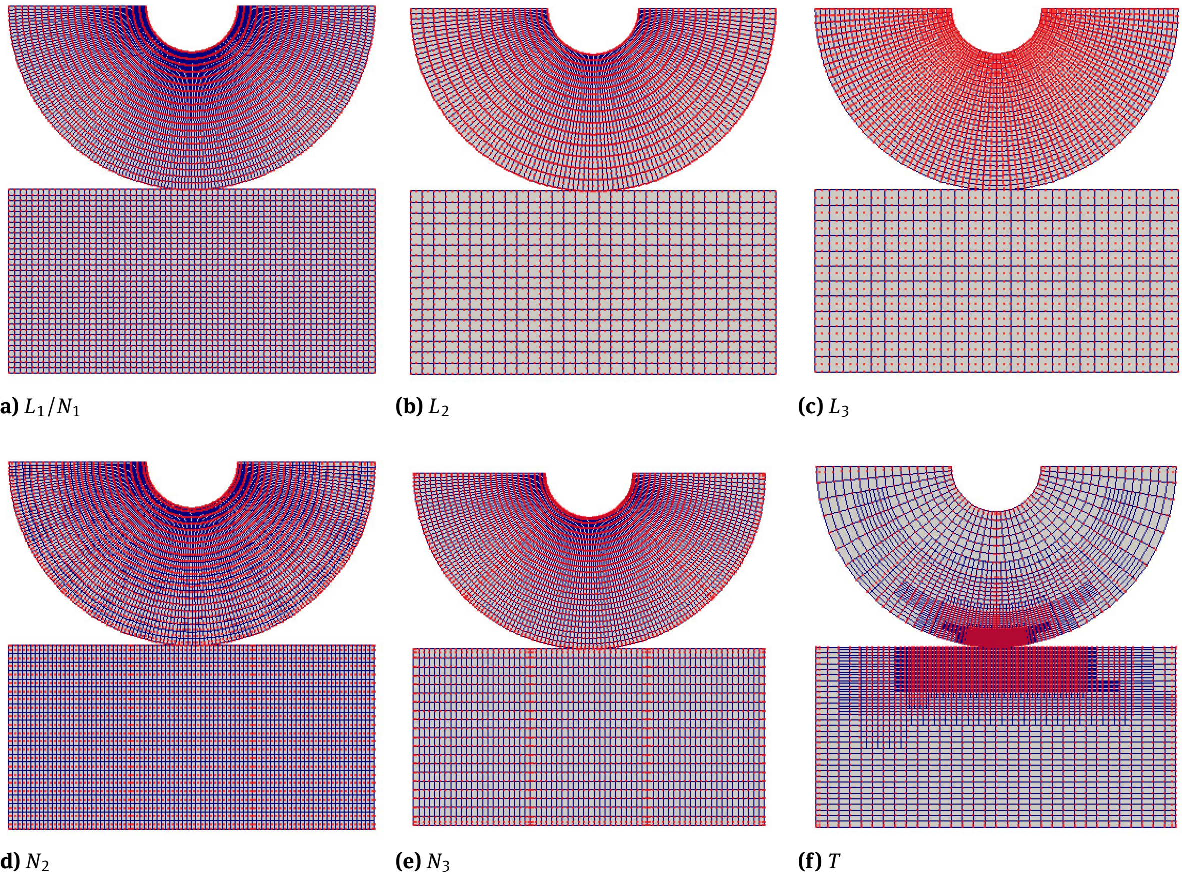

Figure 10: Ironing problem: Lagrange, NURBS, and T-spline meshes. Dof = 11904.

in the surrounding bulk material, with a sequence of artificial snap-through or snap-back branches in the global load-deflection response.

T-splines, NURBS and Lagrange discretizations with the same number of Dofs, or equivalently with the same number of control variables (control points or nodes) are employed and compared. T-splines only encompass third-degree interpolations, whereas for NURBS and Lagrange different degrees are adopted. Once again, cubic T-spline discretizations are denoted by T, while NURBS and Lagrange discretizations with order p in all parametric directions are denoted as Np and Lp, respectively. Lagrange and NURBS meshes are uniform, whereas in the T-spline parameterizations T-junctions are locally added to the meshes near the interfaces. As already done for contact applications, Lagrange and NURBS models are compared with T-spline discretizations for the same number of Dofs, in order to investigate the effect of the different basis functions on performance, and quantify the increase in accuracy obtained through the local refinement capability for a given computational cost.

Three examples are herein presented which consider a 2D double cantilever beam (DCB), and two different 3D peel tests between thin rectangular or triangular laminates. Unless specified otherwise, a fixed number of 2 GPs is adopted for the evaluation of the interface integrals in each surface parametric direction.

5.1 DCB with even bending moments

As first example, a DCB specimen (dimensions 140 x2mm^2 and precrack of 4mm) is loaded in mode-I conditions through an even bending moment (DCB-EBM), M, on the two beams, as employed in experimental investigations on fracture of sandwich specimens, e.g. specimens where two skin layers are joined by a core which is much thinner than the other specimen dimensions (see all the analysed meshes in Fig. 19). An elastic isotropic behaviour is assumed for both bodies, with an elastic modulus $E = 122$ GPa and a Poisson's ratio $\nu = 0.25$. A penalty parameter $\varepsilon_N = 10^5$ MPa/mm is chosen as the default value.

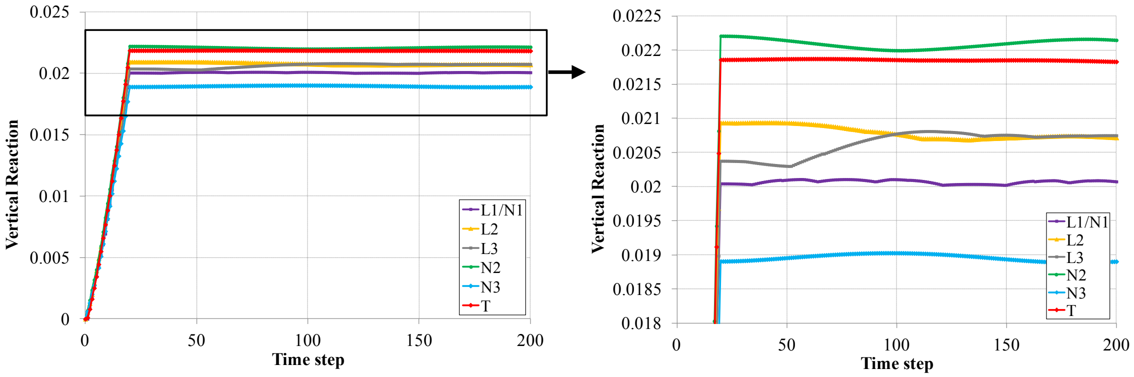

(a) Dof= 1044

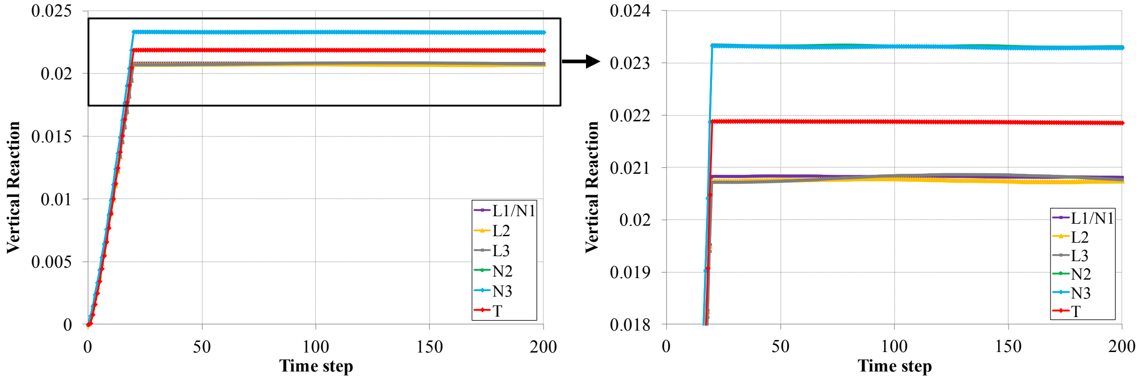

(b) Dof= 3352

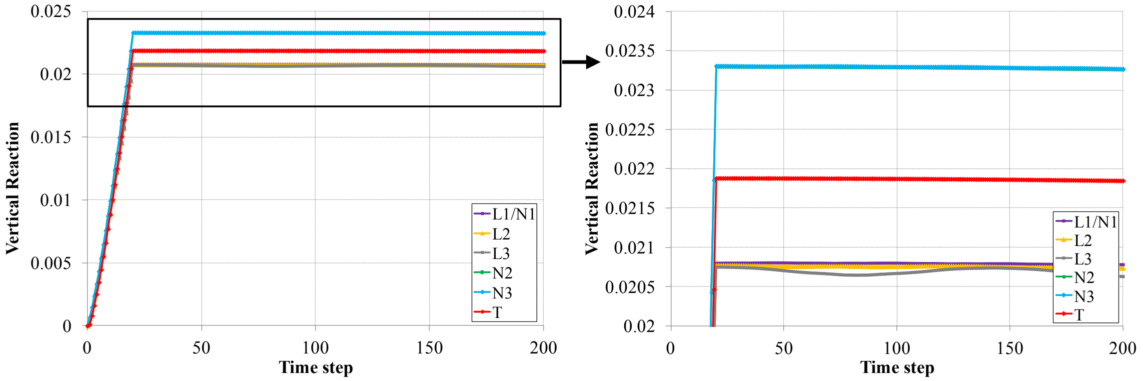

(c) Dof= 11904

Figure 11: Ironing problem: vertical reaction-time response.

A prerequisite for accurate debonding computations is that the element size ahead of the crack tip is sufficiently smaller than the length of the FPZ where the cohesive traction-separation law is activated and the energy is dissipated. While the element size is obviously dictated by the discretization, the length of the FPZ is essentially a function of the CZ parameters.

For such reasons, a low cohesive strength p_{Nmax} = 4 N/mm^2 is herein chosen for a given interfacial fracture energy ϕ_N = 100 N/m in normal direction, in such a way that a sufficiently fine mesh resolution characterizes the FPZ and crack tip singularities can be avoided. As also demonstrated in [68], increasing the cohesive strength leads to more severe irregularities and oscillations in the global response both for Lagrange and NURBS discretizations. In this case, the FPZ would be localized in a smaller region, and higher mesh resolution near the crack tip would be required to improve the results.

The response is herein evaluated in terms of moment-rotation behavior. The numerical results are compared with analytical predictions obtained by combining the concepts of elastic bending theory and LEFM [91]. Note that LEFM can be considered as the limit case of CZ modeling where the cohesive strength tends to infinity and the size of the FPZ accordingly tends to zero, so that the crack tip singularity is recovered. As a result, the moment-rotation response as predicted by LEFM is not expected to agree with the numerically computed response. Nevertheless, the analytical curve is a useful benchmark which is expected to be approached more closely as the cohesive strength is increased.

Linear and higher-order interpolations are first considered with Lagrange and NURBS basis functions, as shown in Figs. 20a,b. More specifically, $L1$ and $L2$ interpolations deliver smooth but too stiff results due to shear locking effects, whereas $L1$ and $N1$ interpolations are herein coincident due to the uniform weights. Conversely, results from higher-order Lagrange parameterizations approximate quite well the analytical results, but featuring large oscillations around a constant value with an irregular and ripetitive pattern. This reflects the transitions between master elements in the process zone which are C^0 continuous.

From a comparison between Figs. 20a and b, NURBS discretizations evidently deliver results of higher quality in comparison with conventional Lagrange finite elements. This is due to the higher (C^{p-1}) order of inter-element continuity achieved with NURBS, as opposed to C^0 in the Lagrange case. The moment-rotation curves obtained from NURBS discretizations are smoother than the Lagrange ones and are nearly unaffected by the interpolation order. These results qualitatively resemble those presented in [16].

The same problem is then solved with locally refined cubic T-spline meshes, whose results are compared with those from cubic Lagrange and NURBS interpolations in Figs. 20a and b. The curves obtained with T-splines approximate very well the analytical results and feature significantly smaller oscillations during the progressive debonding phase (i.e. in the constant branch of the curves) in comparison with those from NURBS interpolations with the same Dofs, as a direct consequence of the locally refined FPZ.

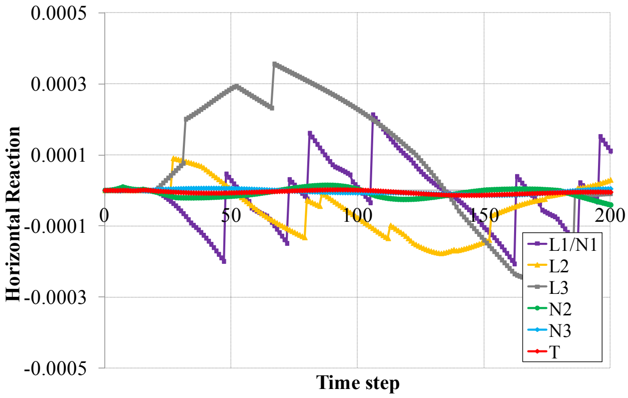

(a) Dof= 1044

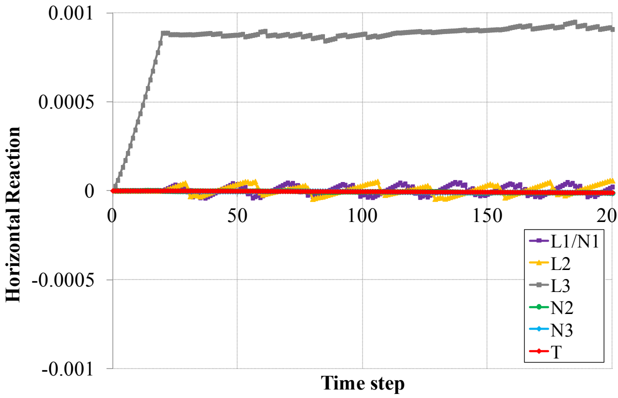

(b) Dof= 3352

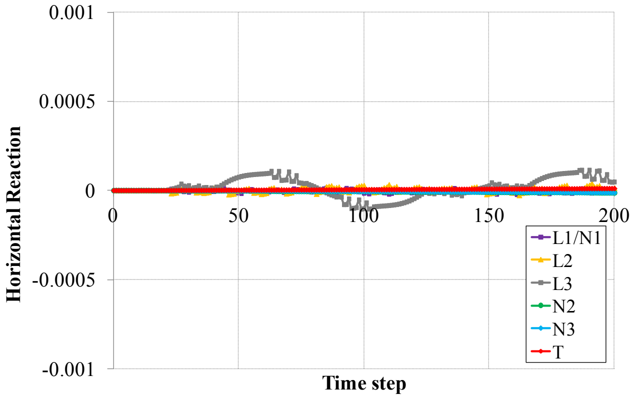

(c) Dof= 11904

Figure 12: Ironing problem: horizontal reaction-time response.

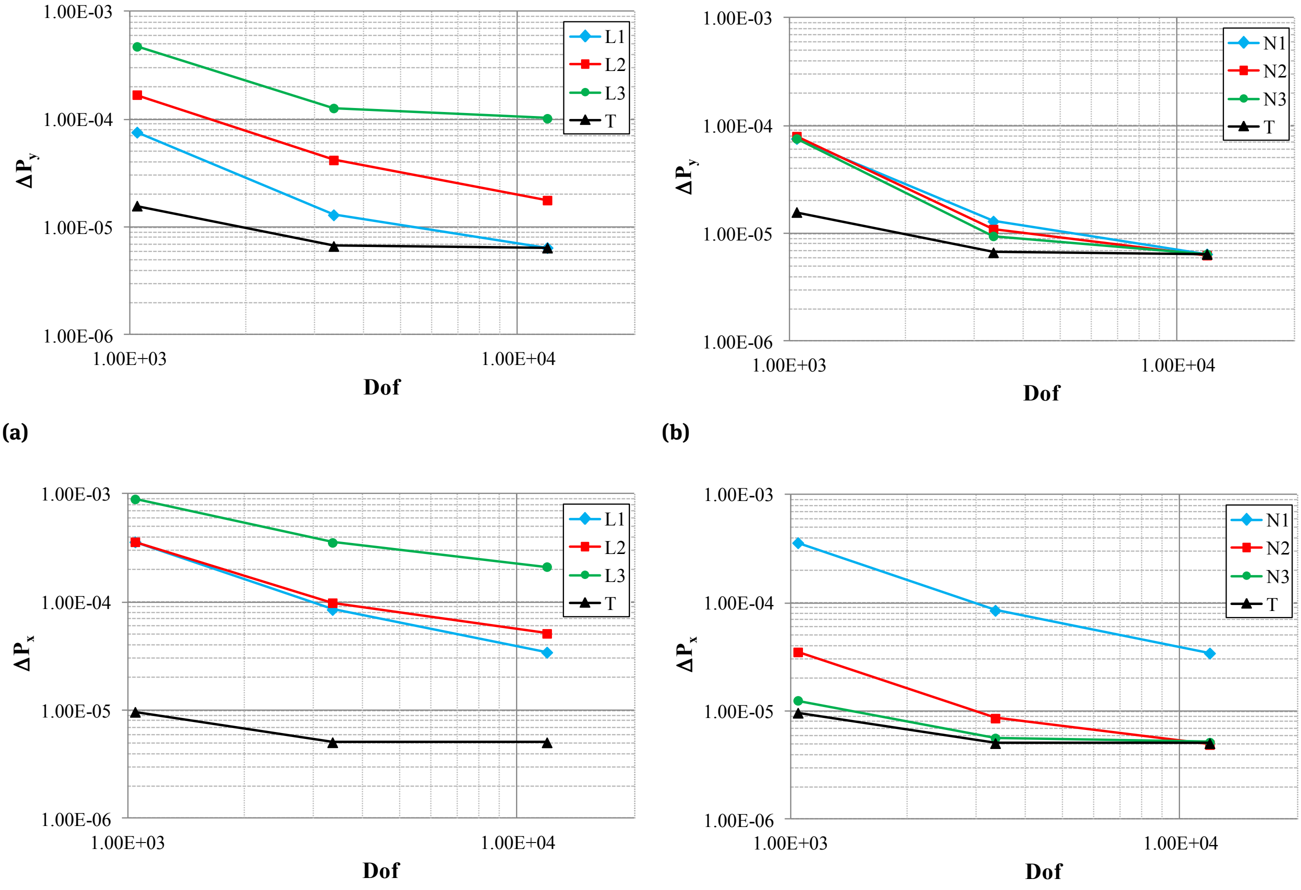

(a) (b) (c) (d)

Figure 13: Ironing problem: amplitude of the vertical (a,b) and the horizontal (c,d) reaction forces for different discretizations.

5.2 3D bimaterial peel test of square laminae

In this section, the T-spline-based integrated contact and CZ formulation is applied to a 3D laminated structure in order to demonstrate the effectiveness of the proposed formulation in conjunction with 3D T-spline discretizations using shell elements for the continuum.

A 3D peel test between two square laminae (dimensions 20 mm x 20 mm x 0.2 mm) is herein analysed. The upper lamina, here considered as slave body, initially bonded to the substrate throughout its length, is peeled away by applying at the left boundary a vertical displacement of 4 mm in 400 time steps, while fixing the two laminae on the right side, as shown in Fig. 21a.

The two laminae are discretized with 3D isogeometric Kirchoff-Love shell elements [90]. Some irregular elements are generated in the T-mesh by including T-junctions around the loaded control point. Also in this case, the analysis is carried out by importing into FEAP the extraction operator generated by the T-spline plugin in the Rhino environment, where the mesh is generated using standard CAD operations. An elastic isotropic material behaviour is assumed for both bodies, with constants $E_1 = 10^6$ MPa and $\nu_1 = 0.3$, for the upper shell and $E_2 = 10^9$ MPa and $\nu_2 = 0.3$ for the lower shell. The lower shell is here treated as master and the upper shell as slave. A bilinear cohesive model with $p_{Nmax} = 10$ MPa and $G_{IC} = 0.3$ N/mm is assigned to the interface to treat peeling.

Fig. 21a shows the deformed mesh at the last time step, after complete debonding, along with the contours of the vertical displacement, whereas the load-deflection history is reported in Fig. 21b in comparison to the analytical results based on the beam theory and LEFM [91]. In the initial loading phase, the two shells are perfectly bonded and the slope of the load-deflection curve corresponds to the stiffness of a single shell having the total thickness of the two laminae. Soon thereafter debonding starts taking place, leading to a decreasing behavior. The subsequent behavior returns to linearity but the stiffness corresponds to that of

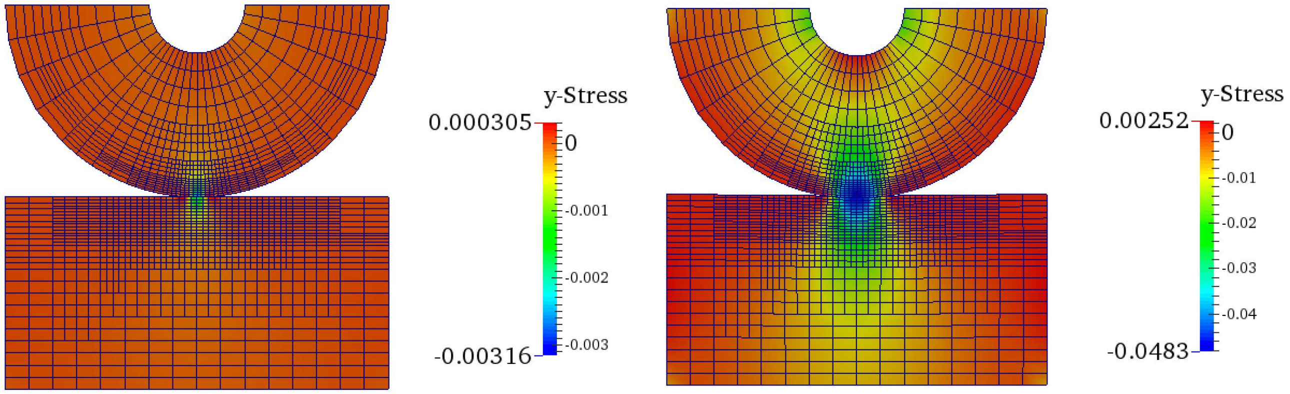

(a) Step 1 **(b)** Step 10

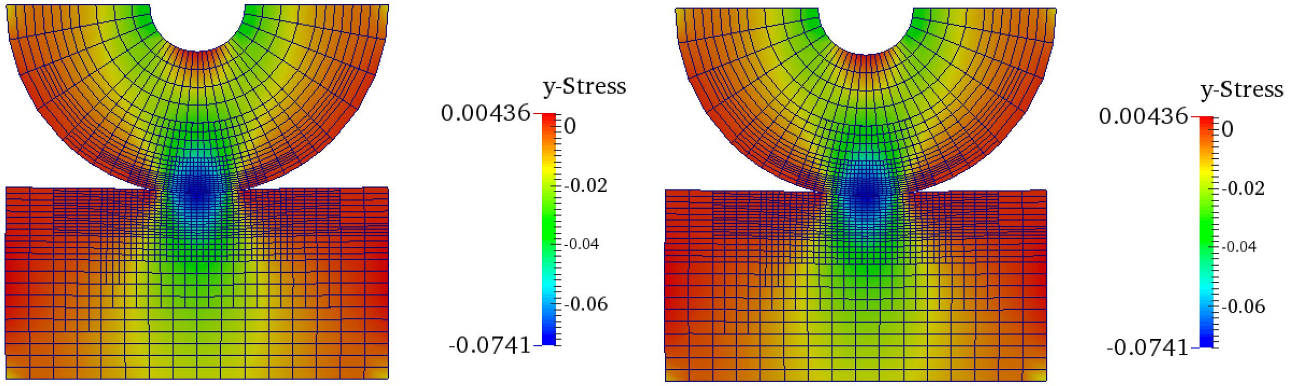

(c) Step 20 **(d)** Step 100

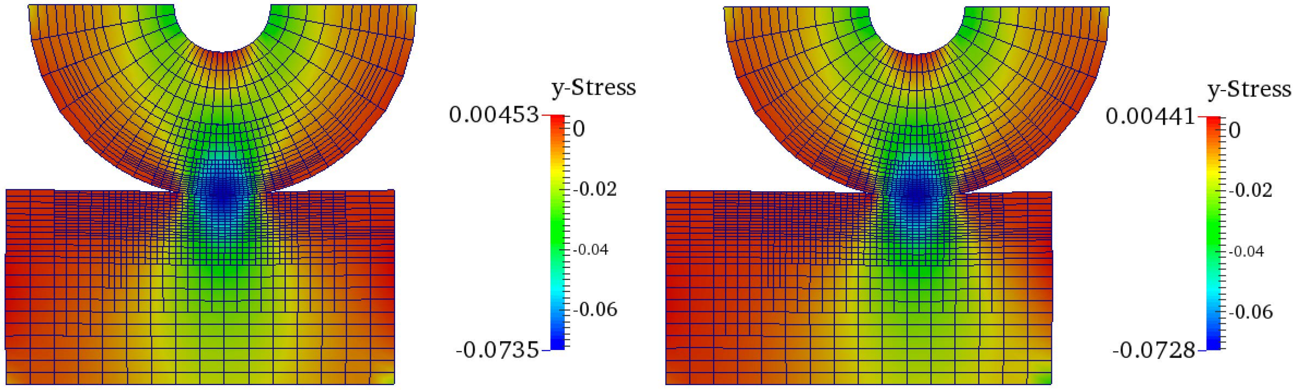

(e) Step 200 **(f)** Step 500

Figure 14: Ironing problem: deformed shape for T-mesh 1. Dof= 1044.

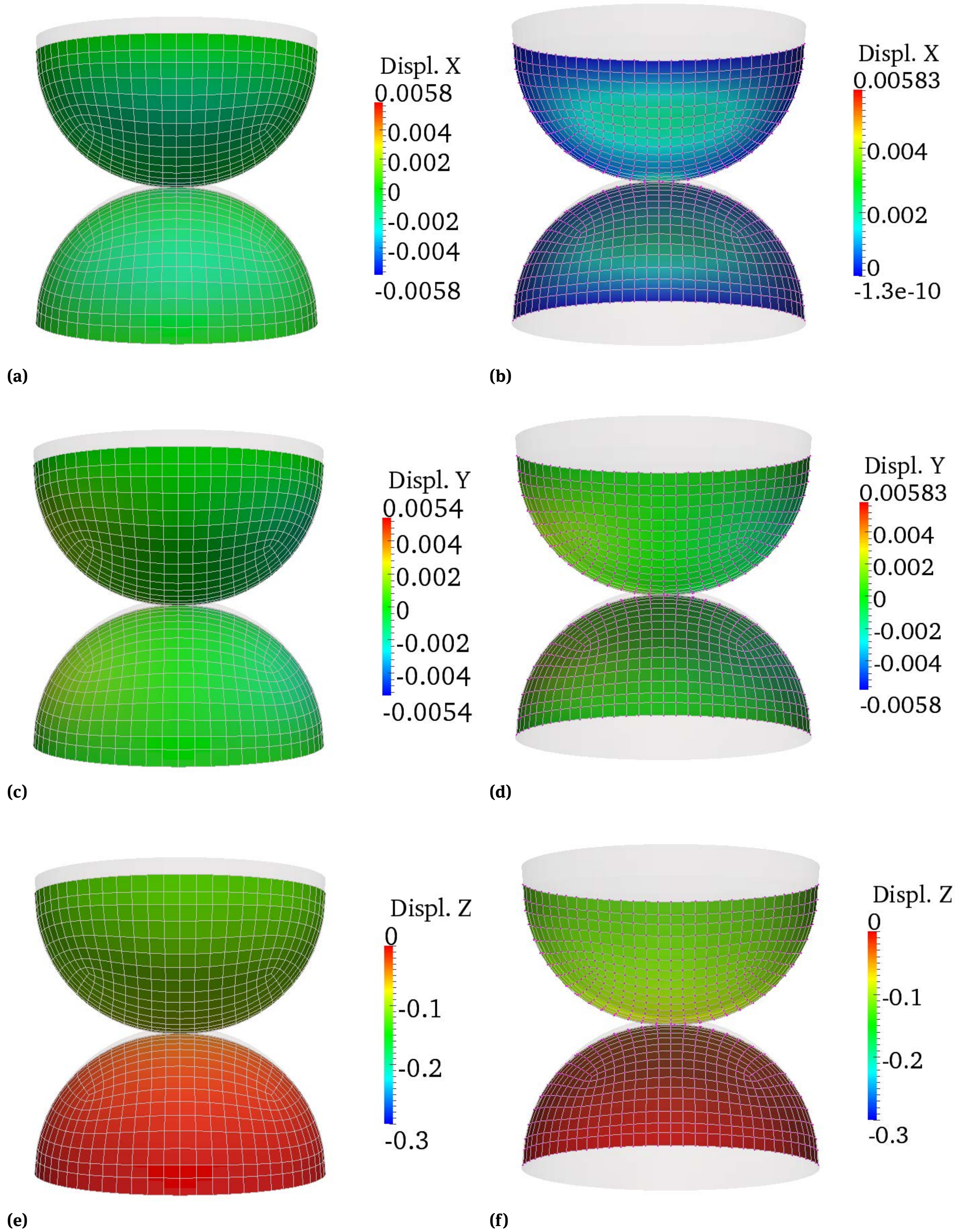

(a) (b) (c) (d) (e) (f)

Figure 15: Hemispheres in normal contact: undeformed and deformed shape and displacement contours for step 5.

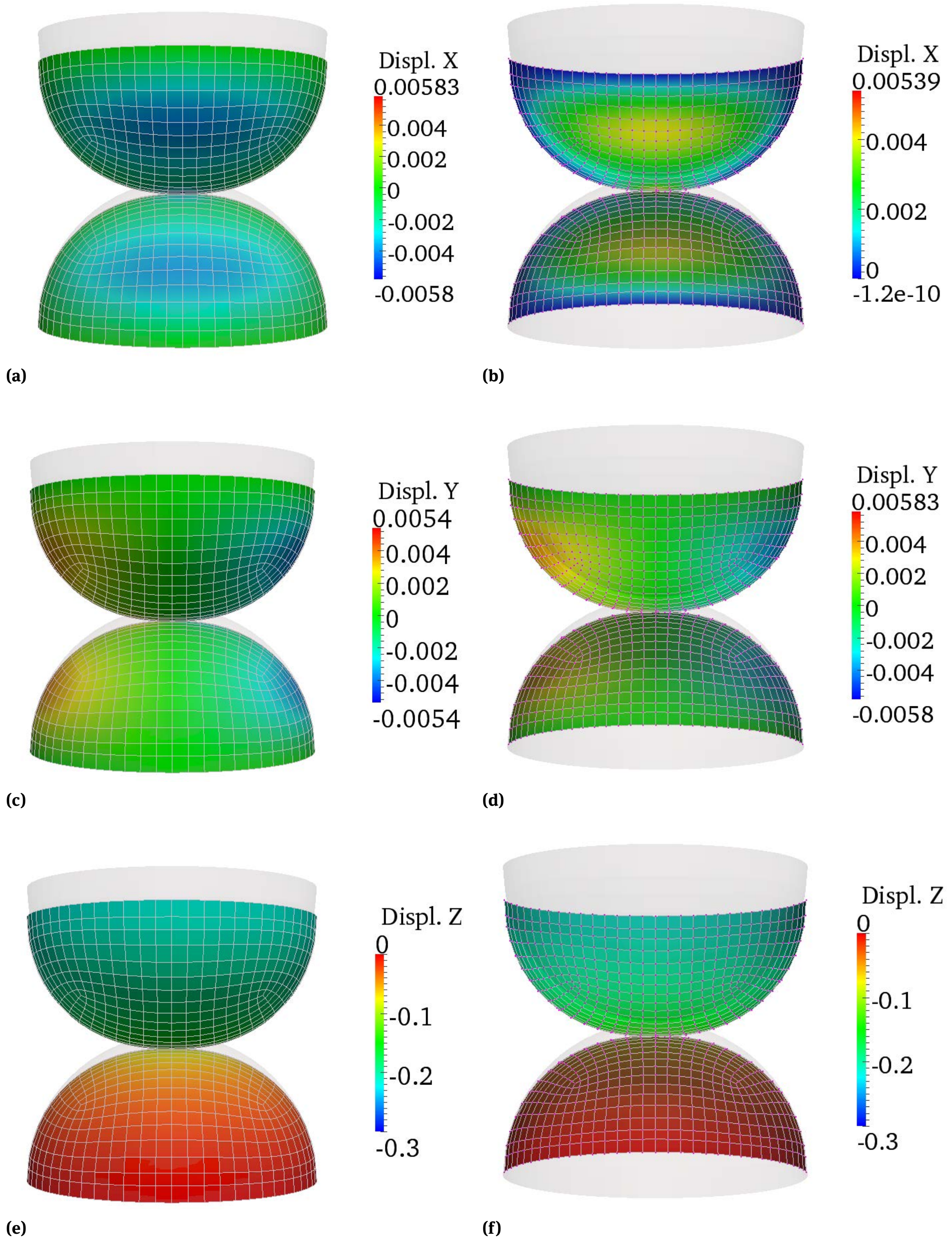

Figure 16: Hemispheres in normal contact: undeformed and deformed shape and displacement contours for step 10.

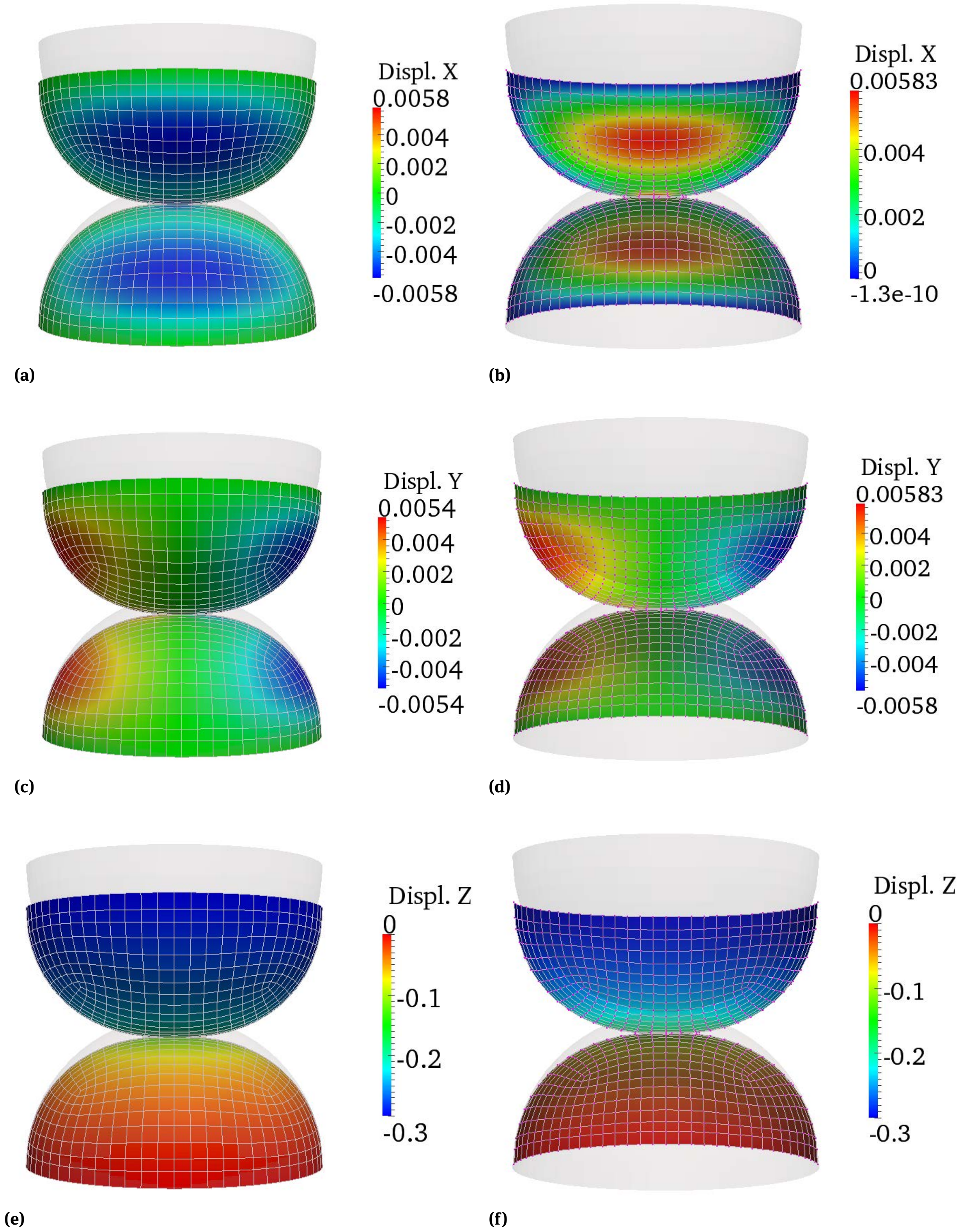

Figure 17: Hemispheres in normal contact: undeformed and deformed shape and displacement contours for step 15.

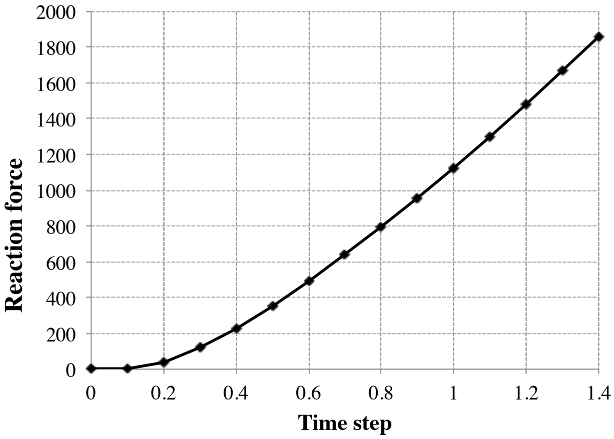

Figure 18: Hemispheres in normal contact: normal reaction history.

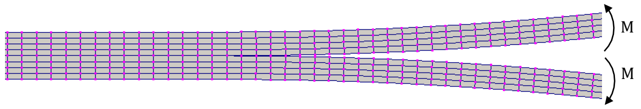

(a) L1

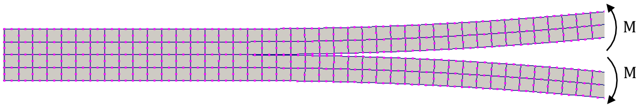

(b) L2

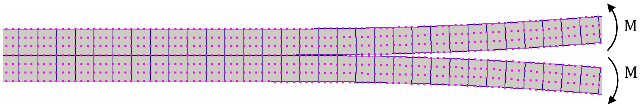

(c) L3

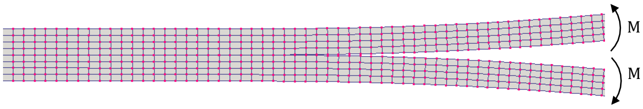

(d) N2

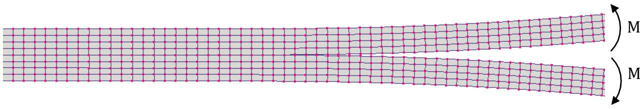

(e) N3

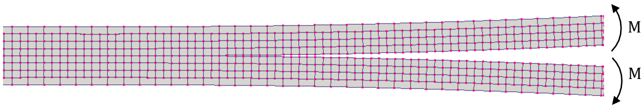

(f) T

Figure 19: DCB-EBM: (a) Lagrange, (b) NURBS, and (c) T-Spline interpolations. Dof= 3700.

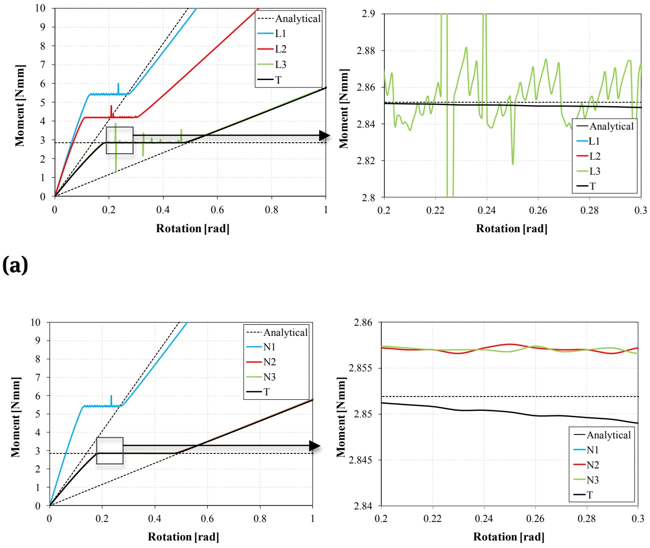

(a)

(b)

Figure 20: DCB-EBM: Load-displacement global response. Comparison of T-Splines with (a) Lagrange and (b) NURBS interpolations. Dof= 3700.

the upper lamina, now fully detached from the lower one. The load-deflection response with 2x2 GPs in the two directions correctly resembles the analytical predictions, and lead only slight oscillations in the descending branch because of the coarsness of the mesh, as visible in the snapshot of Fig. 21b.

This suggests that a C^2 continuity of the interface determines a quite well-resolved deformed FPZ. Due to the large deformation range, the slave GPs are projected onto different master segments as the deformation progresses. However, these transitions occur quite smoothly and do not lead to appreciable oscillations in the global response despite the coarseness of the mesh. An increasing number of GPs, however, is expected to be beneficial in any case, as it improves the resolution in the computation of the cohesive or contact forces, especially for coarse meshes, as herein considered for the T-mesh. The magnitude of the oscillations, indeed, is reduced for increasing number of GPs from 2 up to 8, until macroscopically smooth curves are obtained. These results indicate that increasing the number of interface GPs in the GPTS formulation allows for the use of coarse meshes even when the interface parameters lead to a very small FPZ, thus decreasing the overall computational cost.

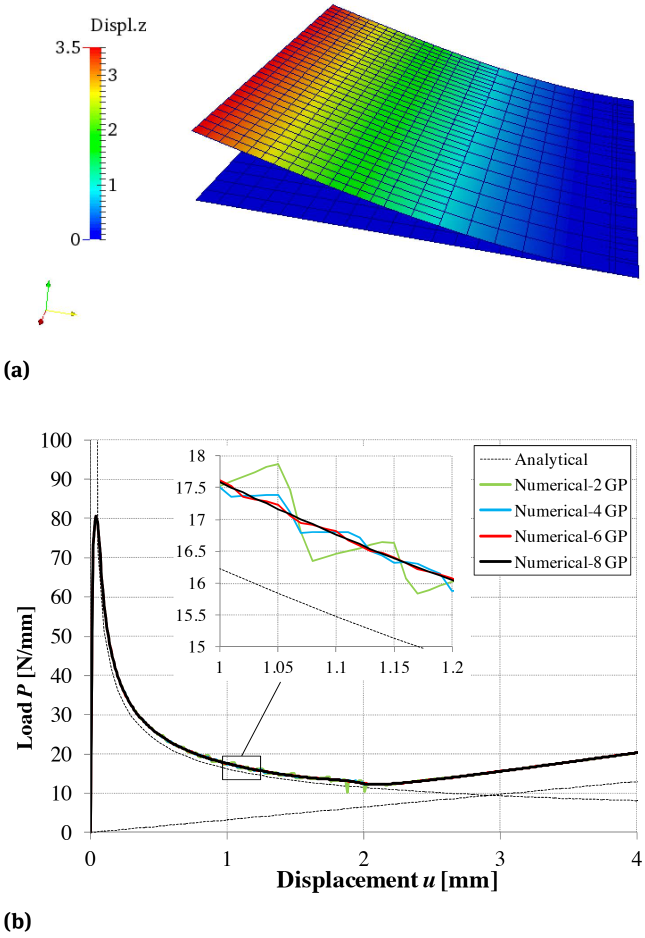

(a)

(b)

Figure 21: 3D thin-walled quadrangular laminates: (a) displacement contour plot after complete dedonding, and (b) load-displacement global response.

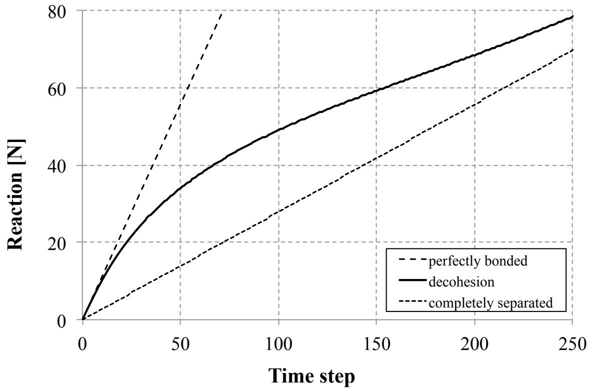

Figure 22: 3D thin-walled triangular laminates: reaction-displacement global response.

5.3 3D debonding of triangular laminae

The last example similarly considers the debonding process of a 3D thin-walled laminated structure of triangular shape. Two equilateral triangular laminae, bonded to each other and fixed on one side, are gradually pulled apart under a concentrated displacement $U_z = 10\,\mathrm{mm}$ applied in 500 time steps to the free corner of each lamina. The two laminae are discretized, once more, with 3D isogeometric Kirchhoff-Love shell elements [90]. Some irregular elements are generated in the T-mesh by including extraordinary points with valence 3 in the T-mesh, leading to a C^1 continuity in the surrounding region and a C^2 continuity in the rest of the domain. An elastic isotropic material behaviour is assumed for both bodies, with constants $E = 10^6$ MPa and $\nu = 0.3$. The lower shell is here treated as master and the upper one as slave. The bilinear cohesive model with $p_{Nmax} = 10\,\mathrm{MPa}$ and $G_{IC} = 0.3\,\mathrm{N/mm}$ is assigned to the interface, as considered in the previous example. The global debonding interactions are monitored through the time step variation of the vertical reaction at the free corner, whose behavior seems to be very smooth despite the relative coarsness of the mesh (see Fig. 22). This is due, once again, to the smooth transitions between adjacent elements guaranteed by the degree of continuity of the T-spline interpolations.

Fig. 23 finally depicts snapshots at different time steps from the response history of the bodies, including the downward displacement contour U_z. In the initial steps the two laminae are perfectly bonded throughout the interface slope of the curve corresponds to the elastic stiffness of the whole laminate. Soon afterwards debonding occurs, leading to a nonlinear behaviour. This is associated to the progressive decohesion of the interface, leading to two separate debonding regions. In the final steps a linear behaviour is observed with a stiffness corresponding to that of the upper lamina, now fully detached from the lower one.

6 Conclusions

This paper summarizes the performance of T-spline-based IGA when applied to frictionless contact and mode-I debonding problems, as compared to NURBS and standard C^0-Lagrange interpolations. The isogeometric discretizations are here incorporated into an existing finite element framework by using Bézier extraction, i.e. a linear operator which maps the Bernstein polynomial basis on Bézier elements to the global isogeometric basis. The

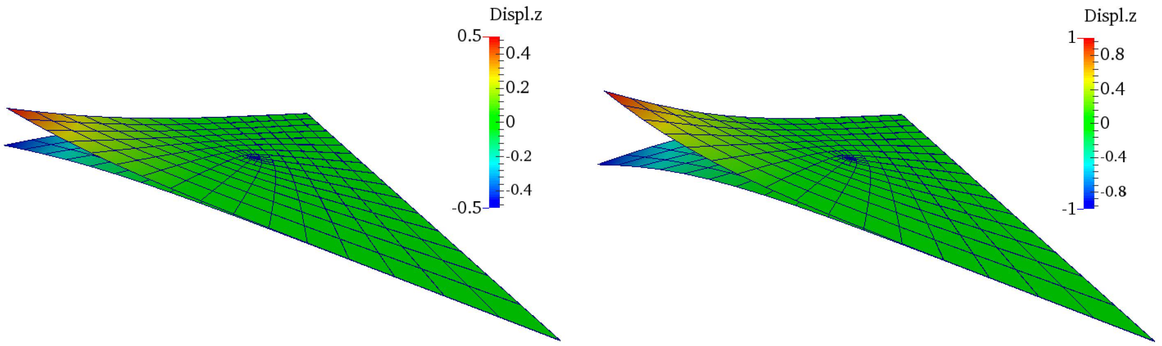

(a) Step 5 **(b)** Step 10

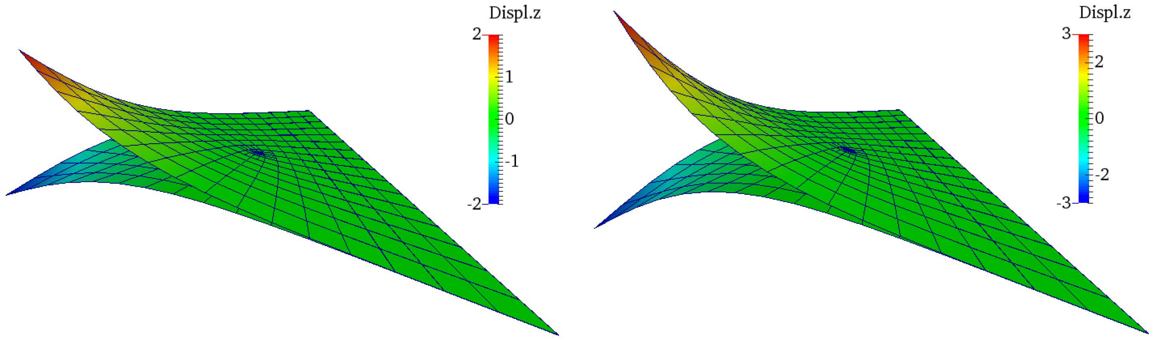

(c) Step 20 **(d)** Step 30

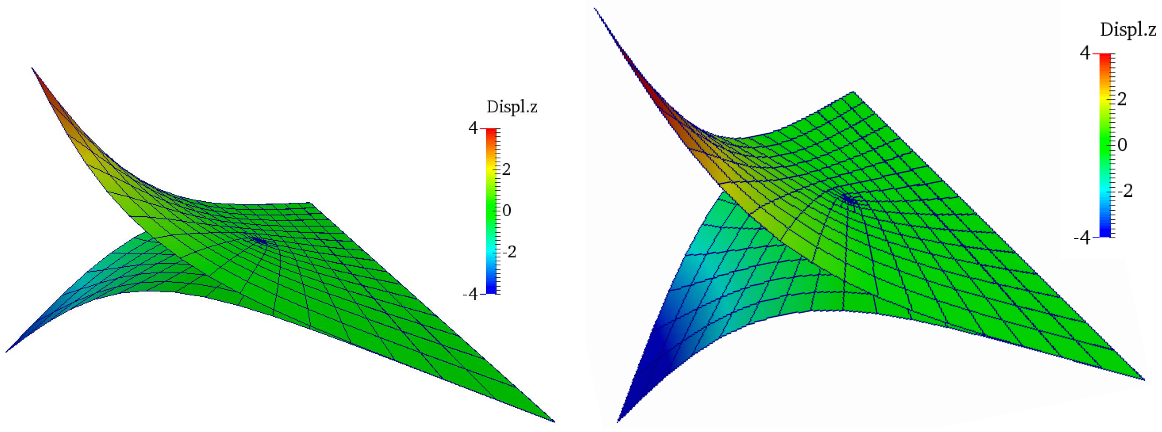

(e) Step 40 **(f)** Step 50

Figure 23: 3D thin-walled triangular laminates with T-Splines: deformed shapes and displacement contours for different time steps.

proposed extended contact and debonding algorithm is based on a GPTS formulation, combined with the penalty method to treat contact constraints in the discretized setting. Some numerical examples show the potential of T-spline IGA to solve challenging contact and debonding problems in 2D and 3D. More specifically, a frictionless ironing problem is first adopted as benchmark to study the performance of T-splines basis functions for contact applications from the standpoint of spatial convergence in comparison to NURBS and Lagrange interpolations. Based on this convergence study, the T-spline error curves are shown to lie always below the NURBS and Lagrange ones for a given number of Dofs. A large deformation 3D example is also herein reported, including a 3D Hertzian problem between two deformable hemispheres, with irregular geometry produced directly in a CAD environment. A smooth and accurate time history of the reaction force is obtained, thus demonstrating the efficiency of T-spline interpolations, due to their local refinement capability together with their ability to represent complex geometries of arbitrary topology as a single watertight parameterization.

The purely geometric enforcement of the non-penetration condition in compression is generalized to encompass both contact and mode-I debonding of interfaces which is here approached through cohesive CZ modelling. Depending on the contact status, an automatic switching procedure is used to choose between cohesive and contact models. The performance of Lagrange, NURBS and T-spline discretizations is evaluated comparatively based on the load-displacement responses from a DCB specimen, a 3D peeling test of a bimaterial laminate, and an edge debonding test between triangular thin laminates.

The results of the Lagrange discretizations are shown to feature oscillations of increasing magnitude and irregularity as the order of the parameterization is increased. These oscillations in turn could lead to important iterative convergence issues. Conversely, the NURBS discretizations lead to smaller oscillations whose magnitude is quite unaffected by the interpolation order within the range of order analysed herein. In any case, T-splines deliver macroscopically smooth results due to their ability of local refinement, which leads to a good resolution of the FPZ in the vicinity of the interface ahead of the cohesive crack. Increasing also the number of interface GPs in the GPTS formulation allows for the use of coarse meshes even when the interface parameters lead to small FPZ, thus decreasing the overall computational cost. As also demonstrated through 3D debonding or peeling examples, the proposed formulation, combined with T-spline isogeometric discretizations featuring high inter-element continuity and local refinement ability, appears to be a computationally accurate and efficient technology for the solution of more complex interface problems. The extension of the developed contact formulation to the frictional setting and to the employment of different contact algorithms is currently underway.

References

[1] Heegaard J.H., Curnier A., An augmented Lagrange method for discrete large slip contact problems, Int. J. Numer. Meth Eng., 1993, 36, 569–593.

[2] Zavarise G., De Lorenzis L., The node-to-segment algorithm for 2D frictionless contact: classical formulation and special cases, Comput. Method. Appl. M., 2009, 198(41-44), 3428–3451.

[3] Pietrzak G., Curnier A., Large deformation frictional contact mechanics: continuum formulation and augmented Lagrangean treatment, Comput. Method. Appl. M., 1999, 177, 351–381.

[4] Taylor R.L., Wriggers P., Smooth surface discretization for large deformation frictionless contact, Technical report, University of California, Berkeley, 1999, Report No. UCB/SEMM-99–04.

[5] Padmanabhan V., Laursen T.A., A framework for development of surface smoothing procedures in large deformation frictional contact analysis, Finite Elem. Anal. Des., 2001, 37, 173–198.

[6] Wriggers P., Krstulovic-Opara L., Korelc J., Smooth C^1–interpolations for twodimensional frictional contact problems, Int. J. Numer. Methods Eng., 2001, 51, 1469–1495.

[7] Krstulovic-Opara L., Wriggers P., Korelc J., A C^1–continuous formulation for 3D finite deformation frictional contact, Comput. Mech., 2002, 29, 27–42.

[8] Lengiewicz J., Korelc J., Stupkiewicz S., Automation of finite element formulations for large deformation contact problems, Int. J. Numer. Methods Eng., 2010, 85, 1252–1279.

[9] Stadler M., Holzapfel G.A., Korelc J., C^n–continuous modelling of smooth contact surfaces using NURBS and application to 2D problems, Int. J. Numer. Methods Eng., 2003, 57, 2177–2203.

[10] Stadler M.,Holzapfel G.A., Subdivision schemes for smooth contact surfaces of arbitrary mesh topology in 3D, Int. J. Numer. Methods Eng., 2004, 60, 1161–1195.

[11] Landon R.L., Hast M.W., Piazza S.J., Robust contact modeling using trimmed nurbs surfaces for dynamic simulations of articular contact, Comput. Meth. Appl. Mech. Eng., 2009, 198, 2339–2346.

[12] Hughes T.J.R., Cottrell J. A., Bazilevs Y., Isogeometric analysis: CAD, finite elements, NURBS, exact geometry, and mesh refinement, Comput. Meth. Appl. Mech. Eng., 2005, 194, 4135–4195.

[13] Temizer İ., Wriggers P., Hughes T.J.R., Contact treatment in isogeometric analysis with NURBS, Comput. Meth. Appl. Mech. Eng., 2011, 200(9–12), 1100–1112.

[14] Temizer İ., Wriggers P., Hughes T.J.R., Three-dimensional mortar-based frictional contact treatment in isogeometric analysis with NURBS, Comput. Meth. Appl. Mech. Eng., 2012, 209–212, 115–128.

[15] Lu J., Isogeometric contact analysis: geometric basis and formulation for frictionless contact, Comput. Meth. Appl. Mech. Eng., 2011, 200, 726–74.

[16] De Lorenzis L., Temizer İ., Wriggers P., Zavarise G., A large deformation frictional contact formulation using NURBS-based isogeometric analysis, Int. J. Numer. Methods Eng., 2011, 87(13), 1278–1300.

[17] De Lorenzis L., Wriggers P., Zavarise G., A mortar formulation for 3D large deformation contact using NURBS-based isogeometric analysis and the augmented Lagrangian method, Comput. Mech., 2012, 49(1), 1–20.

[18] Matzen M.E., Cichosz T., Bischoff M., A point to segment contact formulation for isogeometric, NURBS based finite elements, Comput. Meth. Appl. Mech. Eng., 2013, 255, 27–39.

[19] Dimitri R., De Lorenzis L., Scott M.A., Wriggers P., Taylor R.L., Zavarise G., Isogeometric large deformation frictionless contact using T-splines, Comput. Meth. Appl. Mech. Eng., 2014, 269, 394–414.

[20] De Lorenzis L., Evans J.A., Hughes T.J.R., Reali A., Isogeometric collocation: Neumann boundary conditions and contact, Comput. Meth. Appl. Mech. Eng., 2015, 284, 21–54.

[21] De Lorenzis L., Wriggers P., Hughes T.J.R., Isogeometric contact: a review, GAMM-Mitt. 37, No.1, 2014, 85–123, /DOI 10.1002/gamm.201410005.

[22] Alart P., Curnier A., A mixed formulation for frictional contact problems prone to Newton like solution methods, Comput. Meth. Appl. Mech. Eng., 1991, 92, 353–375.

[23] Cottrell J. A., Hughes T.J.R., Bazilevs Y., Isogeometric Analysis: Toward Integration of CAD and FEA, Wiley, Chichester, 2009.

[24] Bazilevs Y., Calo V.M., Cottrell J.A., Evans J.A., Hughes T.J.R., Lipton S., Scott M.A., Sederberg T.W., Isogeometric analysis using T-splines, Comput. Meth. Appl. Mech. Eng., 2010, 199 (5-8), 229–263.

[25] Fischer K.A., Wriggers P., Frictionless 2D contact formulations for finite deformations based on the mortar method, Comput. Mech., 2005, 36, 226–244.

[26] Kanninen M.F., Popelar C.H., Advanced Fracture Mechanics, Oxford University Press, New York, 1985.

[27] Bažănt Z.P., Planas J., Fracture and Size Effects in Concrete and Other Quasi-Brittle Materials, CRC Press, Boca Raton, 1998.

[28] Rice J.R., A path independent integral and the approximate analysis of strain concentration by notches and cracks, J. Appl. Mech., 1968, 35, 379–386.

[29] Rybicki E.F., Kanninen M.F., A finite element calculation of stress intensity factors by a modified crack closure integral, Eng. Fract. Mech., 1977, 9, 931–938.

[30] Raju I.S., Calculation of strain-energy release rates with higher order and singular finite elements, Eng. Fract. Mech., 1987, 28, 251–274.

[31] Hellen T.K., On the method of virtual crack extensions, Int. J. Numer. Methods Eng., 1975, 9, 187–207.

[32] Griffith A., The phenomena of rupture and flow in solids, Phil. Trans. R. Soc. A., 1921, 221, 163–198.

[33] Thouless M.D., Fracture of a model interface under mixed-mode loading, Acta Metall. Mater., 1990, 38, 1135–1140.

[34] Thouless M.D., Hutchinson J.W., Liniger E.G., Plane-strain, buckling driven delamination of thin films: model experiments and mode-II fracture, Acta Metall. Mater., 1992, 40, 2639–2649.

[35] Natarajan S., Ferreira A.J.M., Nguyen-Xuan H., Analysis of cross-ply laminated plates using isogeometric analysis and unified formulation, Curved and Layer. Struct., 2014, 1, 1–10.

[36] Benzley S.E., Representation of singularities with isoparametric finite elements, Int. J. Numer. Methods Eng., 1974, 8, 537–545.

[37] Gifford L.N., Hilton P.D., Stress intensity factors by enriched finite elements, Eng. Fract. Mech., 1978, 10, 485–496.

[38] Sukumar N., Moran B., Black T., Belytschko T., An element-free galerkin method for three-dimensional fracture mechanics, Comput. Mech., 1997, 20, 170–175.

[39] Jirasek M., Zimmerman T., Embedded crack model: I. basic formulation, Int. J. Numer. Methods Eng., 2001, 50, 1269–1290.

[40] Wells G.N., Sluys L.J., A new method for modelling cohesive cracks using finite elements, Int. J. Numer. Methods Eng., 2001, 50, 2667–2682.

[41] Moës N., Belytschko T., Extended finite element method for cohesive crack growth, Eng. Fract. Mech., 2002, 69, 813–833.

[42] Moës N., Dolbow J., Belytschko T., A finite element method for crack growth without remeshing, Int. J. Numer. Methods Eng., 1999, 46, 131–150.

[43] Sukumar N., Huang Z.Y., Prevost J.H., Suo Z., Partition of unity enrichment for bimaterial interface cracks, Int. J. Numer. Methods Eng., 2004, 59, 1075–1102.

[44] Allix O., Ladeveze P., Interlaminar interface modelling for the prediction of delamination, Compos. Struct., 1992, 22, 235-242.

[45] Schellekens J.C.J., de Borst R., A non-linear finite element approach for the analysis of mode-I free edge delamination in composites, Int. J. Solids Struct., 1993, 30, 1239-1253.

[46] Barenblatt G.I., The formation of equilibrium cracks during brittle fracture. General ideas and hypotheses, Axially-symmetric cracks, J. Appl. Math. Mech., 1959, 23, 622–636.

[47] Dugdale D.S., Yielding of steel sheets containing slits, J. Mech. Phys. Solids, 1960, 8, 100–104.

[48] Needleman A., A continuum model for void nucleation by inclusion debonding, J. Appl. Mech., 1987, 54, 525–531.

[49] Needleman A., An analysis of tensile decohesion along an interface, J. Mech. Phys. Solids, 1990, 38, 289– 324.

[50] Tvergaard V., Hutchinson J.W., The relation between crack growth resistance and fracture process parameters in elastic-plastic solids, J. Mech. Phys. Solids, 1992, 40(6), 1377–1397.

[51] Tvergaard V., Hutchinson J.W., The influence of plasticity on mixed mode interface toughness, J. Mech. Phys. Solids, 1993, 41(6), 1119–1135.

[52] Wei Y., Hutchinson J.W., Interface strength, work of adhesion and plasticity in the peel test, Int. J. Fract., 1998, 93, 315–333.

[53] Corigliano A., Formulation, identification and use of interface models in the numerical analysis of composite delamination, Int. J. Solids Struct., 1993, 30(20), 2779–2811.

[54] Allix O., Ladeveze P., Corigliano A., Damage analysis of interlaminar fracture specimens, Compos. Struct., 1995, 31(1), 61–74.

[55] Point N., Sacco E., A delamination model for laminated composites, Int. J. Solids Struct., 1996, 33(4), 483–509.

[56] Bolzon G., Corigliano A., A discrete formulation for elastic solids with damaging interfaces, Comput. Meth. Appl. Mech. Eng., 1997, 140, 329–359.

[57] Allix O., Corigliano A., Geometrical and interfacial nonlinearities in the analysis of delamination in composites, Int. J. Solids Struct., 1999, 36(15), 2189–2216.

[58] Alfano G., Crisfield M.A., Finite element interface models for the delamination analysis of laminated composites: mechanical and computational issues, Int. J. Numer. Methods Eng., 2001, 50, 1701–1736.

[59] Criesfield M.A., Alfano G., Adaptive hierarchical enrichment for delamination fracture using a decohesive zone model, Int. J. Numer. Methods Eng., 2002, 54, 1369–1390.

[60] Guimatsia I., Ankersen J.K., Davies G.A.O., Iannucci L., Decohesion finite element with enriched basis functions for delamination, Compos. Sci. Technol., 2009, 69(15-16), 2616–2624.

[61] Scott M.A., Borden M.J., Verhoosel C.V., Sederberg T.W., Hughes T.J.R., Isogeometric finite element data structures based on Bézier extraction of T-splines, Int. J. Numer. Methods Eng., 2011, 88(2), 126–156.

[62] Scott M.A., Li X., Sederberg T.W., Hughes T.J.R., Local refinement of analysis-suitable T-splines, Comput. Meth. Appl. Mech. Eng., 2012, 213-216, 206–222.

[63] Li X., Zheng J., Sederberg T.W., Hughes T.J.R., Scott M.A., On linear independence of T-spline blending functions, Comput. Aided Geom. Des., 2012, 29(1), 63–76.

[64] Scott M.A., Simpson R.N., Evans J.A., Lipton S., Bordas S.P.A., Hughes T.J.R., Sederberg T.W., Isogeometric boundary element analysis using unstructured T-splines, Comput. Meth. Appl. Mech. Eng., 2013, 254, 197–221.

[65] Giannelli C., Jüttler B., Speleers H., THB-splines: The truncated basis for hierarchical splines, Comput. Aided Geom. Des., 2012, 29(7), 485–498.

[66] Deng J., Chen F., Li X., Hu C., Tong W., Yang Z., Feng Y., Polynomial splines over hierarchical T-meshes, Graph. Models, 2008, 70, 76–86.

[67] Dokken T., Lyche T., Pettersen K.F., Polynomial splines over locally refined box-partitions, Comput. Aided Geom. Des., 2013, 30(3), 331–356.

[68] Dimitri R., De Lorenzis L., Wriggers P., Zavarise G., NURBS- and T-spline-based isogeoemtric cohesive zone modeling of interface debonding, Comput. Mech., 2014, 54, 369–388.

[69] Sederberg T.W., Zheng J., Bakenov A., Nasri A., T-splines and T-NURCCSs, ACM T. Graphic., 2003, 22(3), 477–484.

[70] Sederberg T.W., Zheng J., Song X., Knot intervals and multi-degree splines, Comput. Aided Geom. Des., 2003, 20, 455–468.

[71] Sederberg T.W., Cardon D.L., Finnigan G.T., North N.S., Zheng J., Lyche T., T-spline simplification and local refinement, ACM T. Graphic., 2004, 23 (3), 276–283.

[72] Cottrell J.A., Reali A., Bazilevs Y., Hughes T.J.R., Isogeometric analysis of structural vibrations, Comput. Meth. Appl. Mech. Eng., 2006, 195, 5257–5296.

[73] Hughes T.J.R., Reali A., Sangalli G., Duality and unied analysis of discrete approximations in structural dynamics and wave propagation: Comparison of p-method nite elements with k-method NURBS, Comput. Meth. Appl. Mech. Eng., 2008, 197(49-50), 4104–4124.

[74] Lorentz G. G., Bernstein Polynomials, Chelsea Publishing Co., New York, 1986.

[75] Piegl L. A., Tiller W., The NURBS Book, Springer, 1996.

[76] Autodesk, 2011, Inc. http://www.tsplines.com/rhino/ .

[77] Schillinger D., Rank E., An unfitted hp-adaptive finite element method based on hierarchical B-splines for interface problems of complex geometry, Comput. Meth. Appl. Mech. Eng., 2011, 200(47-48), 3358– 3380.

[78] Vuong A.V., Giannelli C., Jüttler B., Simeon B., A hierarchical approach to adaptive local refinement in isogeometric analysis, Comput. Meth. Appl. Mech. Eng., 2011, 49-52, 3554– 3567.

[79] Samet H., Foundations of Multidimensional and Metric Data Structures, Morgan Kaufmann Publishers: San Francisco, 2006.

[80] Burstedde C., Wilcox L.C., Ghattas O., p4est: Scalable Algorithms for Parallel Adaptive Mesh Refinement on Forests of Octrees, SIAM J. Sci. Comput., 2011, 33(3), 1103–1133.

[81] Yserantant H., On the multi-level splitting of finite element spaces, Numer. Math., 1986, 49, 379–412.

[82] Krysl P., Grinspun E., Schröder P., Natural hierarchical refinement for finite element methods, Int. J. Numer. Methods Eng., 2003, 56, 1109–1124.

[83] Bungartz H.J., Griebel M., Sparse grids, Acta Numer., 2004, 13, 147–269.

[84] Taylor R.L., FEAP – Finite Element Analysis Program, 2013, www.ce.berkeley/feap, University of California, Berkeley.

[85] Laursen T.A., Computational contact and impact mechanics, 2002, Springer, Berlin.

[86] P. Wriggers, Computational contact mechanics, 2nd edition, 2006, Springer, Berlin.

[87] Puso M.A., Laursen T.A., A mortar segment-to-segment frictional contact method for large deformations, Comput. Meth. Appl. Mech. Eng., 2004, 193, 4891–4913.

[88] Papadopoulos P., Taylor R.L., A mixed formulation for the finite element solution of contact problems, Comput. Meth. Appl. Mech. Eng., 1992, 94(3), 373–389.

[89] Zienkiewicz O.C., Taylor R.L., The Finite Element Method for Solid and Structural Mechanics, 2005, Butterworth-Heinemann, 6th edition.

[90] Kiendl J., Bletzinger K.U., Linhard J., Wüchner R., Isogeometric shell analysis with Kirchhoff-Love elements, Comput. Meth. Appl. Mech. Eng., 2009, 198(49-52), 3902–3914.

[91] Hermes F.H., Process zone and cohesive element size in numerical simulations of delamination in bi-layers, Master thesis, September 24th 2010, MT 10.21, Eindhoven.